Aerospace Science and Technology 153 (2024) 109430

Contents lists available at ScienceDirect

Aerospace Science and Technology

journal homepage: www.elsevier.com/locate/aescte

Active control vibrations of aircraft wings under dynamic loading: Introducing PSO-GWO algorithm to predict dynamical information

Qian Zhang [a], Shaoyong Han [b,*], Mohammed A. El-Meligy [c,d,e], Mehdi Tlija [f]

[a] School of Data Science and Artificial Intelligence, Wenzhou University of Technology, Wenzhou, Zhejiang 325035, China
[b] School of Mathematics and Computer Science, Tongling University, Tongling, Anhui 244061, China
[c] Jadara University Research Center, Jadara University, Jordan
[d] Applied Science Research Center, Applied Science Private University, Amman, Jordan
[e] MEU Research Unit, Middle East University, Amman 11831, Jordan
[f] Department of Industrial Engineering, College of Engineering, King Saud University, P.O. Box 800 Riyadh 11421, Saudi Arabia

ARTICLE INFO

Keywords:
Active control vibrations
Aircraft wings
Dynamic loading
PSO-GWO
Piezoelectric sensor and actuator

ABSTRACT

This study presents an innovative approach to mitigate vibrations induced by external shock on composite structures through the application of an intelligent controller. Leveraging the first-order shear deformation panel theory, a sophisticated controller scheme is developed, integrating methodologies such as the differential quadrature approach and Laplace transform. Furthermore, deep neural network (DNN) and support vector regression (SVR) techniques are employed to enhance prediction accuracy and control efficiency. Additionally, two optimized hybrid models are proposed, incorporating Particle Swarm Optimization (PSO) and Grey Wolf Optimizer (GWO) algorithms, to further refine the controller's performance. The proposed methodology aims to address the challenges associated with vibrations in composite structures by providing a comprehensive and adaptive control solution. By utilizing advanced optimization algorithms and machine learning techniques, the controller can effectively adapt to dynamic changes in external shock conditions, thereby minimizing vibrations and ensuring structural integrity. The integration of ANN and SVR enhances the controller's predictive capabilities, enabling it to anticipate and respond to varying shock scenarios with precision. Through theoretical analysis and numerical simulations, the effectiveness of the proposed intelligent controller is demonstrated in reducing vibrations and enhancing the structural stability of composite systems. The optimized hybrid models, employing PSO and GWO algorithms, further improve the controller's performance by fine-tuning its parameters for optimal control efficiency. Overall, this research contributes to the development of robust control strategies for mitigating vibrations in composite structures subjected to external shock, with potential applications in aerospace, automotive, and civil engineering industries.

1. Introduction

Intelligent controllers are essential in engineering for optimizing system performance and enhancing adaptability across various applications. They improve system accuracy, precision, and response times by adjusting control actions based on real-time data and feedback [1]. This capability is crucial in maintaining desired performance levels in complex systems. Intelligent controllers can dynamically modify control strategies, making them ideal for environments where conditions change frequently. This adaptability is particularly important in industries such as aerospace, automotive, and robotics. By optimizing control actions, these controllers can significantly reduce energy consumption and operational costs, such as in controller systems where they adjust operations based on environmental conditions. They also improve system reliability by detecting and compensating for faults, reducing downtime in critical applications like power grids and medical devices [2].

Intelligent controllers enhance safety in applications by responding quickly to hazardous situations and preventing accidents. They can predict potential failures and take corrective actions, which is vital in safety-critical industries like aviation and nuclear power. Furthermore, they handle complex processes using advanced algorithms, optimizing nonlinear and multivariable systems that traditional controllers cannot manage effectively [3]. They easily integrate with advanced

* Corresponding author.
E-mail address: hanshaoyong@zuaa.zju.edu.cn (S. Han).

https://doi.org/10.1016/j.ast.2024.109430
Received 12 May 2024; Received in revised form 23 July 2024; Accepted 26 July 2024
Available online 31 July 2024

technologies such as the Internet of Things (IoT) and machine learning, enabling smart systems to learn from data and make informed decisions. Many intelligent controllers offer user-friendly interfaces, simplifying system management and allowing easier automation [4]. This reduces operational complexity and enables non-expert users to manage advanced systems efficiently. Additionally, by improving efficiency and performance, they contribute to sustainability by reducing waste, minimizing emissions, and conserving resources. In summary, intelligent controllers are crucial for advancing engineering practices by providing enhanced performance, adaptability, efficiency, and safety [5].

Despite the potential increase in structural stiffness and reduction in vibration amplitudes due to graphene reinforcement, structures incorporating graphene may still experience irregular chaotic vibrations and nonlinear amplitude variations. Nonlinear vibrations are a primary cause of structural failure, underscoring the importance of studying nonlinear vibration control strategies. Shi et al. [6] investigated nonlinear vibration parameters and vibration mitigation in the shafting system of a hydropower unit. They found that a state information vibration controller with higher damping and stiffness factors resulted in more significant vibration reduction. Abbaspour et al. [7] demonstrated that despite system uncertainties induced by temperature fluctuations, a sliding mode controller could restore the fluctuating behavior of graphene-reinforced piezoelectric sandwiched microplates to the desired level. Saeed et al. [8] explored the nonlinear behavior and motion bifurcations of an 8-pole rotor active magnetic bearing system using a novel control technique. Their findings revealed that when the proportional gain of the new controller is low, the rotor system undergoes unstable cyclic oscillation. Mondal et al. [9] investigated the self-excited vibration control of a nonlinear beam using nonlinear resonant time-delay velocity feedback. They observed that the suggested controllers eliminate bifurcations and suppress vibration amplitudes. In a study by Lu et al. [10], PVDF actuators were employed to control high-amplitude vibrations of membranes. They found that the effectiveness of the vibration controller decreased with increasing mode order, pretension, and membrane size. Bauomay et al. [11] explored the efficacy of employing a linear controller to mitigate nonlinear vibration amplitudes in composite plates. Their investigation demonstrated that the controller effectively managed the three-order vibration mode of the plate in terms of its nonlinear vibration amplitude. Introducing an intermediate lumped mass, a novel nonlinear modified positive position feedback method was developed to reduce vibration amplitudes in cantilever beam systems [12]. He et al. [13] employed a smooth-switching linear parameter-varying dynamically output-feedback controller to investigate active vibration suppression in a Blended-Wing-Body flexible aviation wing. Their study revealed that the suggested control strategy significantly reduced the system's abrupt jumps. Zhao et al. [14] studied the control of vibration amplitudes in nonlinear Duffing oscillation systems, finding that linear vibration controllers were less effective compared to those resembling vibration systems. Lu et al. [15] devised a robust control approach to suppress vibration in piezoelectric laminated composite cantilever rectangle plates subjected to aerodynamic forces. Zhu et al. [16] proposed a non-uniform electric field model to intelligently control the vibration of porous piezoelectric conical sandwich structures. Investigating nonlinear vibration reduction in cantilevered rectangular plates using the PPF control approach, Jiang et al. [17] observed optimal vibration control when the frequencies of the PPF controller matched those of the structure naturally. Hu et al. [18] proposed a novel semi-active joint variable stiffness controller to regulate low-frequency vibrations in flexible joint appendages, employing semi-active control methods. Tian et al. [19] addressed nonlinear flutter reduction by periodically inserting nonlinear vibration absorbers into functionally graded plates, observing enhanced flutter stability performance with distributed nonlinear vibration absorbers. Mahesh [20] employed an active restricted layer damping treatment approach to mitigate nonlinear transient vibration amplitudes in sandwich plates with agglomerated FG-CNTs core. Zhao et al. [21] developed a semi-active control mechanism using theory and experimentation to suppress nonlinear vibration in innovative square-celled sandwich plates with a multi-zone magnetorheological elastomers filler core. Additionally, Sahoo et al. [22] utilized high-frequency stimulation to decrease galloping amplitude and eliminate vibration amplitude in elastic components under unstable wind flow conditions.

Stability analysis is crucial in engineering design, ensuring safety by identifying potential failure modes and optimizing performance through efficient material use [23,24]. It guarantees compliance with legal standards and predicts system failure, allowing for preventive maintenance and safe design [25]. In innovative fields like aerospace and civil engineering, stability analysis supports the creation of complex, reliable structures [26]. It balances cost and performance, ensuring economic efficiency and extending the lifespan of systems by withstanding various stresses [27]. Understanding dynamic responses in mechanical systems is essential for smooth operation, while environmental resistance reduces the ecological footprint [28]. Applicable across disciplines, stability analysis is a fundamental aspect of engineering, driving sustainable, durable, and high-performing designs [29]. Analyzing stability ensures that structures and systems have a longer lifespan by withstanding wear and tear, dynamic loads, and environmental stresses, reducing the need for frequent repairs or replacements [30]. In mechanical systems, stability analysis is crucial for understanding the dynamic response to forces and vibrations, which is essential for the smooth and efficient operation of machinery [31]. So, stability analysis is indispensable for creating safe, efficient, and innovative engineering designs that meet regulatory standards, optimize performance, and ensure long-term durability and sustainability [32].

There is no research on the intelligent controller for reducing vibrations caused by external shock on the sandwich doubly curved panel, according to published articles in the literature. So, this study presents an intelligent controller intended to reduce vibrations on composite constructions caused by shock from the outside. A complex controller system is developed by using the first-order shear deformation panel theory and combining the Laplace transform and differential quadrature approaches. In order to improve control efficiency and prediction accuracy, ANN and SVR algorithms are also included. Furthermore, two enhanced hybrid models are suggested, using PSO and GWO algorithms to enhance the controller's functionality even further. The controller can dynamically react to different shock events by using advanced control techniques and optimization algorithms, which reduce vibrations and guarantee structural integrity. Additionally, the controller's predictive skills are improved by the combination of ANN and SVR approaches, allowing it to precisely foresee and react to dynamic changes in external shock circumstances. The hybrid models that have been improved via the integration of PSO and GWO algorithms enhance the controller's performance and guarantee maximum control efficiency. All things considered, the suggested method is a noteworthy development in the subject of structural control and may find use in the civil, automotive, and aerospace engineering sectors. Through efficient exterior shock vibration mitigation, this study enhances the performance, safety, and dependability of composite structures across a range of engineering applications. The novelties of this work can be separated into four fields. 1- Presenting vibration-control equations of the sandwich doubly curved panel under external transient loading. 2- Presenting advanced intelligent controller for mitigating vibrations induced by external shock on the sandwich doubly curved panel. 3- Presenting coupled controller scheme, DQM, and Laplace transform for solving the displacement-time dependent equations. 4- Present innovative outcomes for mitigating vibrations induced by external shock on the sandwich doubly curved panel for future electrical industries.

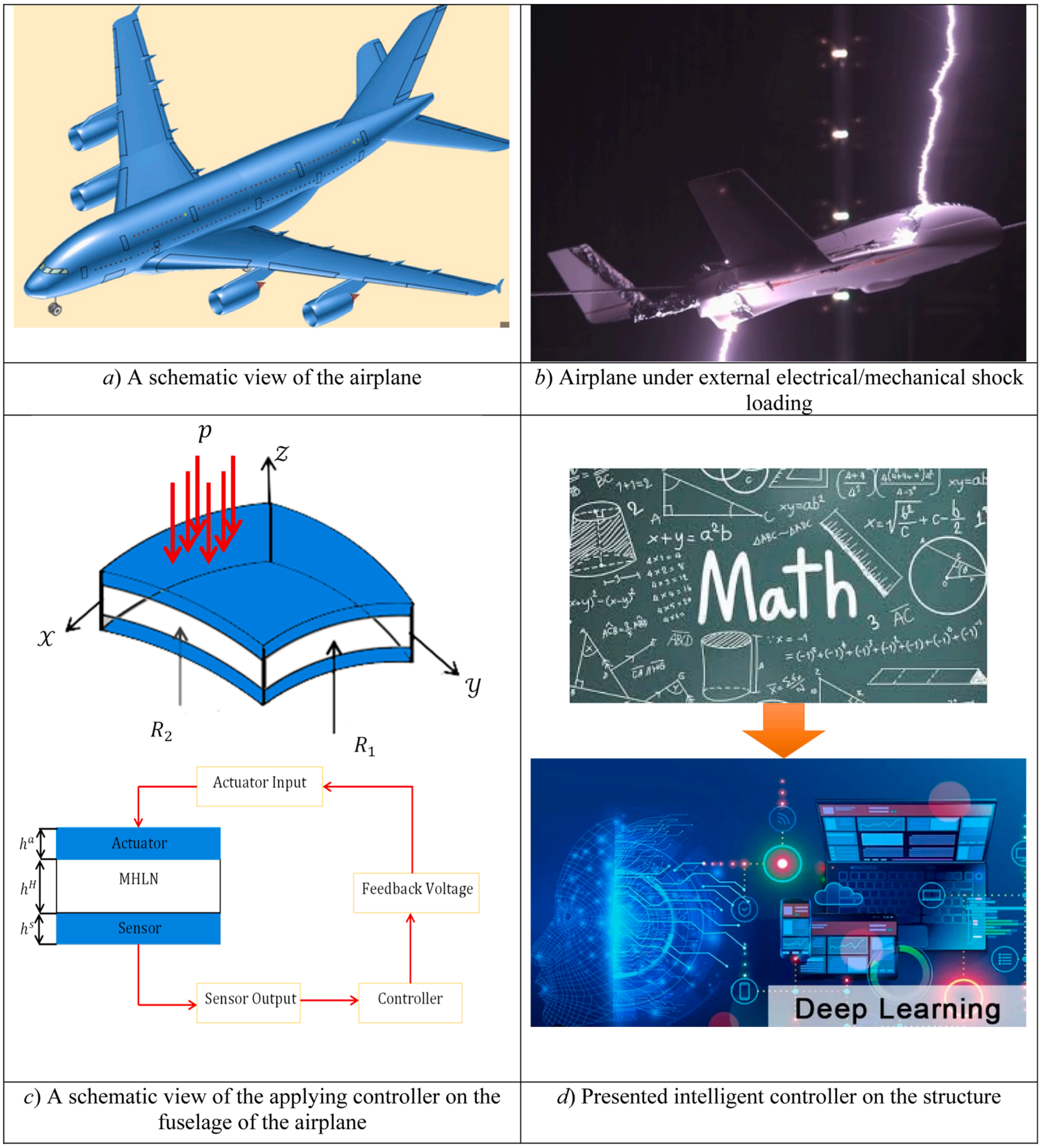

a) A schematic view of the airplane

b) Airplane under external electrical/mechanical shock loading

c) A schematic view of the applying controller on the fuselage of the airplane

d) Presented intelligent controller on the structure

Fig. 1. Showing an intelligence controller for controlling the mitigating vibrations induced by external shock on the fuselage of the airplane.

2. Mathematical modeling

Fig. 1 shows a schematic view of the presented structure, an intelligent controller with geometry conditions. The sensor is embedded in the fuselage structure and continuously monitors the structural response to external shocks (such as pressure pp depicted in the figure). It detects vibrations and measures parameters like displacement, velocity, or acceleration of the fuselage. The sensor outputs the measured data to the controller. This data provides real-time feedback on the structural state of the fuselage. The controller processes the sensor data and determines the necessary corrective actions. It generates a control signal based on the feedback voltage to mitigate the vibrations. The control algorithm can use various control strategies, such as PID control, adaptive control, or more advanced algorithms as presented in neural networks, to compute the appropriate actuator input. The actuator receives the control signal from the controller. It applies forces or moments to the fuselage structure to counteract the detected vibrations. The actuator might use mechanisms like piezoelectric elements, or other smart materials that can dynamically adjust their properties in response to electrical inputs. The input to the actuator is adjusted in real-time to dynamically dampen vibrations. The actuator works to reduce the amplitude of the vibrations by applying forces that oppose the motion induced by the external shocks. The system forms a closed-loop feedback control system, where the sensor continuously provides updated structural response data to the controller. The controller continuously adjusts the actuator inputs based on the real-time data to ensure effective vibration damping. The controller system integrates with the structural dynamics of the fuselage by providing a real-time response to vibrations. This rapid response is crucial for effectively damping vibrations before they can amplify and potentially cause structural damage or discomfort. By constantly monitoring and adjusting the actuator inputs, the system can adapt to varying external shock conditions. This adaptability ensures that the fuselage remains stable under different operational scenarios. The intelligent controller enhances the overall structural integrity of the airplane by reducing the stress and strain induced by vibrations. This prolongs the lifespan of the fuselage and reduces maintenance requirements. In addition to structural benefits, effective vibration damping improves passenger comfort by minimizing the transmission of vibrations to the cabin. By integrating sensors, controllers, and actuators into the fuselage structure, the intelligent controller system forms a comprehensive solution for active vibration control. This integration allows for continuous monitoring and dynamic response, ensuring that vibrations are effectively dampened, enhancing both structural integrity and passenger comfort.

2.1. The homogenization process of MHLN

The two primary components of the homogenization process are the micromechanical theory [33] and the Halpin-Tsai model [34]. The first step involves calculating the composite reinforced with CFs' effective characteristics in the manner described below [35].

$$E_{11} = V_F E_{11}^F + V_{NCM} E^{NCM} \tag{1a}$$

$$\frac{1}{E_{22}} = \frac{V_F}{E_{22}^F} + \frac{V_{NCM}}{E^{NCM}} - V_F V_{NCM} \times \frac{\frac{(\nu^F)^2 E^{NCM}}{E_{22}^F} + \frac{(\nu^{NCM})^2 E_{22}^F}{E^M} - 2\nu^F \nu^{NCM}}{V_F E_{22}^F + V_{NCM} E^{NCM}} \tag{1b}$$

$$\frac{1}{G_{12}} = \frac{V_F}{G_{12}^F} + \frac{V_{NCM}}{G^{NCM}}, G_{23} = G_{12}, G_{13} = G_{12} \tag{1c}$$

$$\rho = V_F \rho^F + V_{NCM} \rho^{NCM} \tag{1d}$$

$$\nu_{12} = V_F \nu^F + V_{NCM} \nu^{NCM} \tag{1e}$$

$$\nu_{21} = \frac{E_{22}}{E_{11}} \nu_{12}, \nu_{13} = \nu_{12}, \nu_{31} = \nu_{21}, \nu_{32} = \nu_{21}, \nu_{23} = \nu_{32} \tag{1f}$$

The relation between V_F and V_{NCM} is as follows:

$$V_F + V_{NCM} = 1 \tag{2}$$

Using the expanded Halpin-Tsai micromechanics, the second phase is structured to determine the effective properties of the CNT-reinforced nanocomposite matrix as follows:

$$E^{NCM} = E^M \left(\frac{5}{8} \left(\frac{1 + 2\beta_{dd} V_{CNT}}{1 - \beta_{dd} V_{CNT}} \right) + \frac{3}{8} \left(\frac{1 + 2(l^{CNT}/d^{CNT}) \beta_{dl} V_{CNT}}{1 - \beta_{dl} V_{CNT}} \right) \right) \tag{3}$$

Here, β_{dd} and β_{dl} would be computed as the following expression.

$$\beta_{dl} = \frac{(E_{11}^{CNT}/E^M) - (d^{CNT}/4t^{CNT})}{(E_{11}^{CNT}/E^M) + (l^{CNT}/2t^{CNT})}, \ \beta_{dd} = \frac{(E_{11}^{CNT}/E^M) - (d^{CNT}/4t^{CNT})}{(E_{11}^{CNT}/E^M) + (d^{CNT}/2t^{CNT})} \tag{4}$$

Base on the W_{CNT}, the CNTs' volume fraction can be given below:

$$V_{CNT}^* = \frac{W_{CNT}}{W_{CNT} + \left(\frac{\rho^{CNT}}{\rho^M} \right)(1 - W_{CNT})} \tag{5}$$

Additionally, the thickness direction and MHLN distribution may be obtained by:

$$V_{CNT} = V_{CNT}^* \tag{6}$$

In addition, the relationship between V_M and V_{CNT} is as follows:

$$V_{CNT} + V_M = 1 \tag{7}$$

Finally, the mechanical properties of the nanocomposite structure may be ascertained using the following methods:

$$\rho^{NCM} = V_{CNT} \rho^{CNT} + V_M \rho^M \tag{8a}$$

$$\nu^{NCM} = \nu^M \tag{8b}$$

$$G^{NCM} = \frac{E^{NCM}}{2(1 + \nu^{NCM})} \tag{8c}$$

Building on Sander's shell theory, Ref. [36] created an FSDT for panel-type structure analysis. This theory is consistent with the moderately thick class of shells and describes displacements on an arbitrary point of the panel $(\overline{\mathscr{U}}, \overline{\mathscr{V}}, \overline{\mathscr{W}})$ as a function of mid-surface displacements $(\mathscr{U}, \ \mathscr{V}, \ \mathscr{W})$ and mid-surface rotations $(\mathscr{I}_{\mathscr{Y}}, \mathscr{I}_{\mathscr{X}})$.

$$\left\{ \begin{array}{c} \overline{\mathscr{U}}(X,Y,Z,t) \\ \overline{\mathscr{V}}(X,Y,Z,t) \\ \overline{\mathscr{W}}(X,Y,Z,t) \end{array} \right\} = \left\{ \begin{array}{c} \left(1 + \frac{\mathscr{Z}}{R_1}\right) U(X,Y,t) \\ \left(1 + \frac{\mathscr{Z}}{R_2}\right) V(X,Y,t) \\ W(X,Y,t) \end{array} \right\} + \mathscr{Z} \left\{ \begin{array}{c} \mathscr{I}_{\mathscr{X}}(X,Y,t) \\ \mathscr{I}_{\mathscr{Y}}(X,Y,t) \\ 0 \end{array} \right\} \tag{9}$$

The modified Sanders shell theory provides several advancements over traditional theories like Reissner and Donnell-Mushtari-Vlasov (DMV) when analyzing panel-type structures, especially under mechanical and electrical loads. Here's how it differs and the advantages it offers:

A. Inclusion of Shear Deformation

Unlike the DMV theory, which neglects transverse shear deformation, the modified Sanders shell theory incorporates it. This allows for a more accurate representation of thick shells or structures where shear effects are significant.

B. Higher-Order Effects:

The modified Sanders theory includes higher-order strain-displacement relations, making it more suitable for analyzing complex stress states and deformations in panels. This contrasts with Reissner's theory, which also considers shear but might not capture higher-order effects as effectively.

C. Electromechanical Coupling:

The theory can integrate electromechanical coupling, making it advantageous for analyzing structures subjected to both mechanical and electrical loads, such as piezoelectric panels. Traditional theories primarily focus on mechanical loads.

D. General Applicability:

The modified Sanders theory is versatile and can be applied to a wide range of boundary conditions and load cases, providing more accurate results for diverse applications compared to DMV, which is more suited to thin shell approximations.

E. Enhanced Accuracy:

By considering both shear deformation and higher-order terms, the modified Sanders theory offers improved accuracy for predicting deflections, stresses, and strains in complex geometries and loading scenarios, leading to better structural analysis and design optimization. Overall, these enhancements make the modified Sanders shell theory a powerful tool for analyzing modern engineering structures, providing better insight into their behavior under multifaceted loading conditions.

Generally speaking, the modified Sanders shell theory used in this study is a particular example of the Reissner, Donnell–Mushtari–Valasov, and Sanders theories. To get a concise summary of the Reissner, Sanders, DMV, and modified Sanders shell theories, one may consult Chaudhuri and Kabir's publications [37]. With the displacement field and the modified Sander's theory assumptions [38], the linear strain–displacement relations are found as follows.

$$\begin{Bmatrix} \mathscr{E}_{\mathscr{X}\mathscr{X}} \\ \mathscr{E}_{\mathscr{Y}\mathscr{Y}} \\ \mathscr{L}_{\mathscr{Y}\mathscr{Z}} \\ \mathscr{L}_{\mathscr{X}\mathscr{Z}} \\ \mathscr{L}_{\mathscr{X}\mathscr{Y}} \end{Bmatrix} = \begin{bmatrix} \dfrac{\partial}{\partial \mathscr{X}} & 0 & \dfrac{1}{R_1} & \mathscr{Z}\dfrac{\partial}{\partial \mathscr{X}} & 0 \\ 0 & \dfrac{\partial}{\partial \mathscr{Y}} & \dfrac{1}{R_2} & 0 & \mathscr{Z}\dfrac{\partial}{\partial \mathscr{Y}} \\ 0 & -\dfrac{1}{R_2} & \dfrac{\partial}{\partial \mathscr{Y}} & 0 & 1 \\ -\dfrac{1}{R_1} & 0 & \dfrac{\partial}{\partial \mathscr{X}} & 1 & 0 \\ (1+\mathscr{Z}c_0)\dfrac{\partial}{\partial \mathscr{Y}} & (1-\mathscr{Z}c_0)\dfrac{\partial}{\partial \mathscr{X}} & 0 & \mathscr{Z}\dfrac{\partial}{\partial \mathscr{Y}} & \mathscr{Z}\dfrac{\partial}{\partial \mathscr{X}} \end{bmatrix} \begin{Bmatrix} U \\ V \\ W \\ \mathscr{f}_{\mathscr{X}} \\ \mathscr{f}_{\mathscr{Y}} \end{Bmatrix} \tag{10}$$

where the components of shear strain, $\mathscr{L}_{ij}$, and normal strain, $\mathscr{E}_{ij}$, are, respectively. Not to mention, $c_0 = \frac{1}{2}\left(\frac{1}{R_1} - \frac{1}{R_2}\right)$. The Sander's shell theory feature that is used to account for the condition of zero strain for rigid body motion is this constant [38].

According to Hooke's elasticity, the MHLN layer's stress-strain equations may be expressed as follows [39]

$$\begin{Bmatrix} \sigma_{\mathscr{X}\mathscr{X}} \\ \sigma_{\mathscr{Y}\mathscr{Y}} \\ \tau_{\mathscr{Y}\mathscr{Z}} \\ \tau_{\mathscr{X}\mathscr{Z}} \\ \tau_{\mathscr{X}\mathscr{Y}} \end{Bmatrix} = \left[\overline{\mathscr{T}}_{11}\overline{\mathscr{T}}_{12}000\overline{\mathscr{T}}_{21}\overline{\mathscr{T}}_{22}00000\overline{\mathscr{T}}_{44}00000\overline{\mathscr{T}}_{55}00000\overline{\mathscr{T}}_{66} \right] \begin{Bmatrix} \mathscr{E}_{\mathscr{X}\mathscr{X}} \\ \mathscr{E}_{\mathscr{Y}\mathscr{Y}} \\ \mathscr{L}_{\mathscr{Y}\mathscr{Z}} \\ \mathscr{L}_{\mathscr{X}\mathscr{Z}} \\ \mathscr{L}_{\mathscr{X}\mathscr{Y}} \end{Bmatrix} \tag{11}$$

In which

$$\overline{\mathscr{T}}_{11} = \mathscr{T}_{22}\sin^4\theta + 2(\mathscr{T}_{12} + 2\mathscr{T}_{66})\sin^2\theta\cos^2\theta + \mathscr{T}_{11}\cos^4\theta \tag{12}$$

$$\overline{\mathscr{T}}_{12} = \mathscr{T}_{12}(\cos^4\theta + \sin^4\theta) + (\mathscr{T}_{22} + \mathscr{T}_{11} - 4\mathscr{T}_{66})\cos^2\theta\sin^2\theta$$

$$\overline{\mathscr{T}}_{22} = \mathscr{T}_{11}\sin^4\theta + \mathscr{T}_{22}\cos^4\theta + 2\mathscr{T}_{12}\sin^2\theta\cos^2\theta + 2(\mathscr{T}_{12} + 2\mathscr{T}_{66})\cos^2\theta\sin^2\theta$$

$$\overline{\mathscr{T}}_{44} = \mathscr{T}_{55}\sin^2\theta + \mathscr{T}_{44}\cos^2\theta$$

$$\overline{\mathscr{T}}_{55} = \mathscr{T}_{44}\sin^2\theta + \mathscr{T}_{55}\cos^2\theta$$

$$\overline{\mathscr{T}}_{66} = \mathscr{T}_{66}(\cos^2\theta - \sin^2\theta)^2 - 4(2\mathscr{T}_{12} - \mathscr{T}_{11} - \mathscr{T}_{22})\cos^2\theta\sin^2\theta$$

The terms involved in Eq. (12) would be obtained as [39]:

$$\mathscr{T}_{11} = \frac{E_{11}}{(1-\upsilon_{12}\upsilon_{21})}, \mathscr{T}_{12} = \frac{\upsilon_{12}E_{11}}{(1-\upsilon_{12}\upsilon_{21})}, \mathscr{T}_{22} = \frac{E_{22}}{(1-\upsilon_{12}\upsilon_{21})} \tag{13}$$

$$\mathscr{T}_{66} = G_{12}, \mathscr{T}_{55} = G_{13}, \mathscr{T}_{44} = G_{23}$$

The panel's constitutive equations with the linear piezo electro-elastic effects included may be expressed as [40]

$$\begin{Bmatrix} \sigma_{\mathscr{X}\mathscr{X}} \\ \sigma_{\mathscr{Y}\mathscr{Y}} \\ \tau_{\mathscr{Y}\mathscr{Z}} \\ \tau_{\mathscr{X}\mathscr{Z}} \\ \tau_{\mathscr{X}\mathscr{Y}} \end{Bmatrix} = \begin{bmatrix} \mathscr{T}_{11} & \mathscr{T}_{12} & 0 & 0 & 0 \\ \mathscr{T}_{21} & \mathscr{T}_{22} & 0 & 0 & 0 \\ 0 & 0 & \mathscr{T}_{44} & 0 & 0 \\ 0 & 0 & 0 & \mathscr{T}_{55} & 0 \\ 0 & 0 & 0 & 0 & \mathscr{T}_{66} \end{bmatrix} \begin{Bmatrix} \mathscr{E}_{\mathscr{X}\mathscr{X}} \\ \mathscr{E}_{\mathscr{Y}\mathscr{Y}} \\ \mathscr{L}_{\mathscr{Y}\mathscr{Z}} \\ \mathscr{L}_{\mathscr{X}\mathscr{Z}} \\ \mathscr{L}_{\mathscr{X}\mathscr{Y}} \end{Bmatrix} - \begin{bmatrix} 0 & 0 & e_{31} \\ 0 & 0 & e_{32} \\ 0 & e_{24} & 0 \\ e_{15} & 0 & 0 \\ 0 & 0 & 0 \end{bmatrix} \begin{Bmatrix} E_{\mathscr{X}} \\ E_{\mathscr{Y}} \\ E_{\mathscr{Z}} \end{Bmatrix} \tag{14}$$

$$\begin{Bmatrix} D_{\mathscr{X}} \\ D_{\mathscr{Y}} \\ D_{\mathscr{Z}} \end{Bmatrix} = \begin{bmatrix} 0 & 0 & 0 & e_{15} & 0 \\ 0 & 0 & e_{24} & 0 & 0 \\ e_{31} & e_{32} & 0 & 0 & 0 \end{bmatrix} \begin{Bmatrix} \mathscr{E}_{\mathscr{X}\mathscr{X}} \\ \mathscr{E}_{\mathscr{Y}\mathscr{Y}} \\ \mathscr{L}_{\mathscr{Y}\mathscr{Z}} \\ \mathscr{L}_{\mathscr{X}\mathscr{Z}} \\ \mathscr{L}_{\mathscr{X}\mathscr{Y}} \end{Bmatrix} + \begin{bmatrix} \eta_1 & 0 & 0 \\ 0 & \eta_2 & 0 \\ 0 & 0 & \eta_3 \end{bmatrix} \begin{Bmatrix} E_{\mathscr{X}} \\ E_{\mathscr{Y}} \\ E_{\mathscr{Z}} \end{Bmatrix}.$$

$$\mathscr{T}_{11} = \frac{E}{1-\upsilon^2}, \mathscr{T}_{12} = \frac{\upsilon E}{1-\upsilon^2}, \mathscr{T}_{22} = \frac{E}{1-\upsilon^2}, \mathscr{T}_{44} = \mathscr{T}_{55} = \mathscr{T}_{66} = \frac{E}{2(1+\upsilon)}$$

In Eq. (14), electric displacement coefficients, dielectric permittivity coefficients, elements of the electric field vector, piezoelectric constants, elastic constants, shear stress components, and normal stress components are introduced via D_i, η_i, E_i, e_{ij}, $\mathscr{T}_{ij}$, τ_{ij}, and σ_{ij}, respectively. The negative gradient of the electric potential yields the components of the electric field for each of the piezoelectric layers [41]. Electric potential may be seen as a linear function of the thickness coordinate when piezoelectric layers are sufficiently thin. A three-dimensional layerwise finite elements analysis is used in [42] to support this assumption for thin piezoelectric layers. Additionally, because only the transverse electrical field is prominent, other components of the in-plane electrical field across the piezoelectric layers are ignored [41]. As a result, the electric fields for the two layers may be expressed as follows:

$$\begin{Bmatrix} E^a_{\mathscr{X}} \\ E^a_{\mathscr{Y}} \\ E^a_{\mathscr{Z}} \\ E^s_{\mathscr{X}} \\ E^s_{\mathscr{Y}} \\ E^s_{\mathscr{Z}} \end{Bmatrix} = \begin{bmatrix} 0 & 0 \\ 0 & 0 \\ \dfrac{-1}{h^a} & 0 \\ 0 & 0 \\ 0 & 0 \\ 0 & \dfrac{-1}{h^s} \end{bmatrix} \begin{Bmatrix} \Phi^a \\ \Phi^s \end{Bmatrix} \tag{15}$$

Here, the electric potential difference function between the two surfaces of the actuator and sensor layers is denoted by Φ^s and Φ^a, respectively. Φ^s and Φ^a denote the electric potential of the top surface of the sensor and actuator, respectively, when the bottom surface of each piezoelectric layer is grounded. The stress resultants are connected to the stresses by the equations when $\mathscr{Z}/R_1$ and $\mathscr{Z}/R_2$ are insignificant in contrast with unity, based on the shallow shell FSDT (which accepts the requirements $h/R_1,\ h/R_2\ <\ 0.05$ [43]).

$$(\mathscr{n}_{\mathscr{X}\mathscr{X}},\mathscr{n}_{\mathscr{Y}\mathscr{Y}},\mathscr{n}_{\mathscr{X}\mathscr{Y}}) = \int_{-\frac{1}{2}h^H - h^s}^{-\frac{1}{2}h^H} (\sigma_{\mathscr{X}\mathscr{X}},\sigma_{\mathscr{Y}\mathscr{Y}},\tau_{\mathscr{X}\mathscr{Y}})d\mathscr{Z} + \int_{-\frac{1}{2}h^H}^{\frac{1}{2}h^H} (\sigma_{\mathscr{X}\mathscr{X}},\sigma_{\mathscr{Y}\mathscr{Y}},\tau_{\mathscr{X}\mathscr{Y}})d\mathscr{Z} + \int_{\frac{1}{2}h^H}^{\frac{1}{2}h^H + h^a} (\sigma_{\mathscr{X}\mathscr{X}},\sigma_{\mathscr{Y}\mathscr{Y}},\tau_{\mathscr{X}\mathscr{Y}})d\mathscr{Z} \tag{16}$$

$$(\mathscr{m}_{\mathscr{X}\mathscr{X}},\mathscr{m}_{\mathscr{Y}\mathscr{Y}},\mathscr{m}_{\mathscr{X}\mathscr{Y}}) = \int_{-\frac{1}{2}h^H - h^s}^{-\frac{1}{2}h^H} \mathscr{Z}(\sigma_{\mathscr{X}\mathscr{X}},\sigma_{\mathscr{Y}\mathscr{Y}},\tau_{\mathscr{X}\mathscr{Y}})d\mathscr{Z} + \int_{-\frac{1}{2}h^H}^{\frac{1}{2}h^H} \mathscr{Z}(\sigma_{\mathscr{X}\mathscr{X}},\sigma_{\mathscr{Y}\mathscr{Y}},\tau_{\mathscr{X}\mathscr{Y}})d\mathscr{Z} + \int_{\frac{1}{2}h^H}^{\frac{1}{2}h^H + h^a} \mathscr{Z}(\sigma_{\mathscr{X}\mathscr{X}},\sigma_{\mathscr{Y}\mathscr{Y}},\tau_{\mathscr{X}\mathscr{Y}})d\mathscr{Z}$$

$$(\mathscr{q}_{\mathscr{X}\mathscr{Z}},\mathscr{q}_{\mathscr{Y}\mathscr{Z}}) = K_s \int_{-\frac{1}{2}h^H - h^s}^{-\frac{1}{2}h^H} (\tau_{\mathscr{X}\mathscr{Z}},\tau_{\mathscr{Y}\mathscr{Z}})d\mathscr{Z} + K_s \int_{-\frac{1}{2}h^H}^{\frac{1}{2}h^H} (\tau_{\mathscr{X}\mathscr{Z}},\tau_{\mathscr{Y}\mathscr{Z}})d\mathscr{Z} + K_s \int_{\frac{1}{2}h^H}^{\frac{1}{2}h^H + h^a} (\tau_{\mathscr{X}\mathscr{Z}},\tau_{\mathscr{Y}\mathscr{Z}})d\mathscr{Z}$$

The shear correction factor is denoted by K_s. Since it is well acknowledged that the value of 5/6 may be used to estimate K_s for composite plates and panels [44], the shear correction factor for the hybrid shell panel in this study is $K_s\ = 5/6$.

3. Equations of motion

Using the Hamilton principle [45–47], the equations of motion for a hybrid doubly curved panel are determined. This principle states that the following equality must exist for a point in the structures to be in equilibrium.

$$\int_0^{t_1} (\delta U_e + \delta U_s + \delta V - \delta K)dt = 0 \tag{17}$$

where δU_s, δU_e, δV and δK stand for the virtual strain energy, virtual electrical energy, virtual work performed by externally applied forces, and virtual kinetic energy of the current system, respectively. For a panel-type construction, the previously mentioned purposes become [41,48]

$$\delta U_s = \int_{\mathscr{Z}}\int_A (\sigma_{\mathscr{X}\mathscr{X}}\delta\mathscr{E}_{\mathscr{X}\mathscr{X}} + \sigma_{\mathscr{Y}\mathscr{Y}}\delta\mathscr{E}_{\mathscr{Y}\mathscr{Y}} + \sigma_{\mathscr{X}\mathscr{Y}}\delta\mathscr{L}_{\mathscr{X}\mathscr{Y}} + K_s\tau_{\mathscr{X}\mathscr{Z}}\delta\mathscr{L}_{\mathscr{X}\mathscr{Z}} + K_s\tau_{\mathscr{Y}\mathscr{Z}}\delta\mathscr{L}_{\mathscr{Y}\mathscr{Z}})dAd\mathscr{Z} \tag{18}$$

$$\delta U_e = -\int_{\mathscr{Z}}\int_A (D^a_{\mathscr{Z}}\delta E^a_{\mathscr{Z}} + D^s_{\mathscr{Z}}\delta E^s_{\mathscr{Z}})dAd\mathscr{Z}$$

$$\delta V = -\int_A (p\delta\mathscr{W} + q^a\delta\Phi^a)dA$$

$$\delta K = \int_{\mathscr{Z}}\int_A \rho\left\{\left[\left(1+\frac{\mathscr{Z}}{R_1}\right)\dot{\mathscr{U}} + \mathscr{Z}\dot{f}_{\mathscr{X}}\right]\left[\left(1+\frac{\mathscr{Z}}{R_1}\right)\delta\dot{\mathscr{U}} + \mathscr{Z}\delta\dot{f}_{\mathscr{X}}\right] + \left[\left(1+\frac{\mathscr{Z}}{R_2}\right)\dot{\mathscr{V}} + \mathscr{Z}\dot{f}_{\mathscr{Y}}\right]\left[\left(1+\frac{\mathscr{Z}}{R_2}\right)\delta\dot{\mathscr{V}} + \mathscr{Z}\delta\dot{f}_{\mathscr{Y}}\right] + \dot{\mathscr{W}}\delta\dot{\mathscr{W}}\right\}dAd\mathscr{Z}$$

The external mechanical applied load and the surface charge density applied to the actuator layer are denoted by $p = F_0H(t)$ and q^a, respectively, in function δV. Since the sensor layer is often not activated externally, this word is not present in δV. The following system of equations of motion is obtained by going back to Eq. (15), replacing Eq. (18) with Eq. (17), and using the Green-Gauss theorem to alleviate the virtual displacements.

$$\delta\mathscr{U} : n_{\mathscr{X}\mathscr{X},\mathscr{X}} + n_{\mathscr{X}\mathscr{Y},\mathscr{Y}} + c_0 m_{\mathscr{X}\mathscr{Y},\mathscr{Y}} + \frac{q_{\mathscr{X}\mathscr{Z}}}{R_1} = \left(S_1 + \frac{2}{R_1}S_2\right)\ddot{\mathscr{U}} + \left(S_2 + \frac{1}{R_1}S_3\right)\ddot{f}_{\mathscr{X}} \tag{19}$$

$$\delta\mathscr{V} : n_{\mathscr{X}\mathscr{Y},\mathscr{X}} + n_{\mathscr{Y}\mathscr{Y},\mathscr{Y}} - c_0 m_{\mathscr{X}\mathscr{Y},\mathscr{X}} + \frac{q_{\mathscr{Y}\mathscr{Z}}}{R_2} = \left(S_1 + \frac{2}{R_2}S_2\right)\ddot{\mathscr{V}} + \left(S_2 + \frac{1}{R_2}S_3\right)\ddot{f}_{\mathscr{Y}}$$

$$\delta\mathscr{W} : \mathscr{T}_{\mathscr{X}\mathscr{Z},\mathscr{X}} + \mathscr{T}_{\mathscr{Y}\mathscr{Z},\mathscr{Y}} - \frac{\mathscr{n}_{\mathscr{X}\mathscr{X}}}{R_1} - \frac{\mathscr{n}_{\mathscr{Y}\mathscr{Y}}}{R_2} + p = S_1\ddot{\mathscr{W}}$$

$$\delta f_{\mathscr{X}} : m_{\mathscr{X}\mathscr{X},\mathscr{X}} + m_{\mathscr{X}\mathscr{Y},\mathscr{Y}} - q_{\mathscr{X}\mathscr{Z}} = \left(S_2 + \frac{1}{R_1}S_3\right)\ddot{\mathscr{U}} + S_3\ddot{f}_{\mathscr{X}}$$

$$\delta f_{\mathscr{Y}} : m_{\mathscr{X}\mathscr{Y},\mathscr{X}} + m_{\mathscr{Y}\mathscr{Y},\mathscr{Y}} - q_{\mathscr{Y}\mathscr{Z}} = \left(S_2 + \frac{1}{R_2}S_3\right)\ddot{\mathscr{V}} + S_3\ddot{f}_{\mathscr{Y}}$$

$$\delta\Phi^a : \frac{1}{h^a}\int_{\frac{1}{2}h^H}^{\frac{1}{2}h^H + h^a} D^a_{\mathscr{Z}}d\mathscr{Z} = q^a$$

$$\delta\Phi^s : \frac{1}{h^s}\int_{-\frac{1}{2}h^H - h^s}^{-\frac{1}{2}h^H} D^s_{\mathscr{Z}} d\mathscr{Z} = 0$$

where $S_i = I_i + h^a H_i^a + h^s H_i^s$ and $I_i = \int_{-\frac{1}{2}h^H - h^s}^{-\frac{1}{2}h^H} \mathscr{Z}^{i-1}\rho(\mathscr{Z})d\mathscr{Z} + \int_{-\frac{1}{2}h^H}^{\frac{1}{2}h^H} \mathscr{Z}^{i-1}\rho(\mathscr{Z})d\mathscr{Z} + \int_{\frac{1}{2}h^H}^{\frac{1}{2}h^H + h^a} \mathscr{Z}^{i-1}\rho(\mathscr{Z})d\mathscr{Z}, i = 1,2,3.$

We solely address the immovable clamped-supported edge circumstances and the moveable simply-supported edge conditions in this study. This is one way to write mathematical formulas for this type of edge support: Movable simply-supported edge:

$$\mathscr{U}(\mathscr{X},0,t) = \mathscr{U}(\mathscr{X},b,t) = 0,\ \mathscr{V}(0,\mathscr{Y},t) = \mathscr{V}(a,\mathscr{Y},t) = 0 \tag{20}$$

$$\mathscr{m}_{\mathscr{Y}\mathscr{Y}}(\mathscr{X},0,t) = \mathscr{m}_{\mathscr{Y}\mathscr{Y}}(\mathscr{X},b,t) = 0,\ \mathscr{m}_{\mathscr{X}\mathscr{X}}(0,\mathscr{Y},t) = \mathscr{m}_{\mathscr{X}\mathscr{X}}(a,\mathscr{Y},t) = 0$$

$$\not{\ }_{\mathscr{X}}(\mathscr{X},0,t) = \not{\ }_{\mathscr{X}}(\mathscr{X},b,t) = 0,\ \not{\ }_{\mathscr{Y}}(0,\mathscr{Y},t) = \not{\ }_{\mathscr{Y}}(a,\mathscr{Y},t) = 0$$

$$\mathscr{W}(\mathscr{X},0,t) = \mathscr{W}(\mathscr{X},b,t) = 0,\ \mathscr{W}(0,\mathscr{Y},t) = \mathscr{W}(a,\mathscr{Y},t) = 0$$

$$\mathscr{n}_{\mathscr{Y}\mathscr{Y}}(\mathscr{X},0,t) = \mathscr{n}_{\mathscr{Y}\mathscr{Y}}(\mathscr{X},b,t) = 0,\ \mathscr{n}_{\mathscr{X}\mathscr{X}}(0,\mathscr{Y},t) = \mathscr{n}_{\mathscr{X}\mathscr{X}}(a,\mathscr{Y},t) = 0$$

$$\Phi^a(\mathscr{X},0,t) = \Phi^a(\mathscr{X},b,t) = 0,\ \Phi^a(0,\mathscr{Y},t) = \Phi^a(a,\mathscr{Y},t) = 0$$

$$\Phi^s(\mathscr{X},0,t) = \Phi^s(\mathscr{X},b,t) = 0,\ \Phi^s(0,\mathscr{Y},t) = \Phi^s(a,\mathscr{Y},t) = 0$$

Immovable clamped-supported edge

$$\mathscr{U}(\mathscr{X},0,t) = \mathscr{U}(\mathscr{X},b,t) = 0,\ \mathscr{U}(0,\mathscr{Y},t) = \mathscr{U}(a,\mathscr{Y},t) = 0 \tag{21}$$

$$\mathscr{V}(\mathscr{X},0,t) = \mathscr{V}(\mathscr{X},b,t) = 0,\ \mathscr{V}(0,\mathscr{Y},t) = \mathscr{V}(a,\mathscr{Y},t) = 0$$

$$\mathscr{W}(\mathscr{X},0,t) = \mathscr{W}(\mathscr{X},b,t) = 0,\ \mathscr{W}(0,\mathscr{Y},t) = \mathscr{W}(a,\mathscr{Y},t) = 0$$

$$\not{\ }_{\mathscr{X}}(\mathscr{X},0,t) = \not{\ }_{\mathscr{X}}(\mathscr{X},b,t) = 0,\ \not{\ }_{\mathscr{X}}(0,\mathscr{Y},t) = \not{\ }_{\mathscr{X}}(a,\mathscr{Y},t) = 0$$

$$\not{\ }_{\mathscr{Y}}(\mathscr{X},0,t) = \not{\ }_{\mathscr{Y}}(\mathscr{X},b,t) = 0,\ \not{\ }_{\mathscr{Y}}(0,\mathscr{Y},t) = \not{\ }_{\mathscr{Y}}(a,\mathscr{Y},t) = 0$$

$$\Phi^a(\mathscr{X},0,t) = \Phi^a(\mathscr{X},b,t) = 0,\ \Phi^a(0,\mathscr{Y},t) = \Phi^a(a,\mathscr{Y},t) = 0$$

$$\Phi^s(\mathscr{X},0,t) = \Phi^s(\mathscr{X},b,t) = 0,\ \Phi^s(0,\mathscr{Y},t) = \Phi^s(a,\mathscr{Y},t) = 0$$

3.1. Controller scheme

This study uses a constant-gain negative velocity feedback control technique that links the direct and inverse piezoelectric effects in a closed-loop system to provide feedback control of the integrated doubly curved structure. Many different kinds of buildings employ this controller for buckling and vibration control [41,49]. The aforementioned control law's mathematical formulation is

$$\Phi^a = -G_{\mathscr{V}}\dot{\Phi}^s \tag{22}$$

In this instance, the velocity feedback control gain is shown as $G_{\mathscr{V}}$.

4. Solution through Numerical Method

The main procedures for using the DQA to arrive at a numerical answer are described in this section.

4.1. Differential quadrature approach (DQA)

According to DQA, a one-dimensional function's p$^{\text{th}}$ derivative may be obtained as [50–52]

$$\frac{\partial^p \mathscr{T}(\mathscr{X})}{\partial \mathscr{X}^p} = \sum_{j=1}^{\mathscr{N}_{\mathscr{X}}} \Re_{sj}^{(p)}\mathscr{T}(\mathscr{X}_j) for\ s = 1,2,\ldots,\mathscr{N}_{\mathscr{X}} \tag{23}$$

here $\Re_{sj}^{(p)}$ signifies the weight coefficients for the s^{th} grid-point $(j = 1,2,\ldots,\mathscr{N}_{\mathscr{X}})$ and $\mathscr{N}_{\mathscr{X}}$ signifies the grid-points' total number.

Employing Eq. (24), $\Re_{sj}^{(p)}$ for $s \neq j$ will be achieved as [53]

$$\Re_{sj}^{(p)} = p\left(\Re_{ss}^{(p-1)}\Re_{sj}^{(1)} - \frac{\Re_{sj}^{(p-1)}}{\mathscr{X}_s - \mathscr{X}_j}\right), p = 2,3,\ldots,\mathscr{N}_{\mathscr{X}} - 1 and\ s,j = 1,2,\ldots,\mathscr{N}_{\mathscr{X}} \tag{24}$$

here $\Re_{sj}^{(1)}$ would be formulated by the next relation [53]

$$\Re_{sj}^{(1)} = \frac{\mathscr{M}^{(1)}(\mathscr{X}_s)}{(\mathscr{X}_s - \mathscr{X}_j)\mathscr{M}^{(1)}(\mathscr{X}_j)}, s,j = 1,2,\ldots,\mathscr{N}_{\mathscr{X}} \tag{25}$$

Next relationship would be employed to acquire $\mathscr{A}_{sj}^{(p)}$

$$\Re_{ss}^{(p)} = -\sum_{j=1, j\neq s}^{\mathscr{N}_{\mathscr{X}}} \Re_{sj}^{(p)}, s = 2,3,\ldots,\mathscr{N}_{\mathscr{X}}\ and\ p = 1,2,\ldots,\mathscr{N}_{\mathscr{X}} - 1 \tag{26}$$

One can derive $\mathscr{M}^{(1)}$ in Eq. (25) as

$$\mathscr{M}^{(1)}(\mathscr{X}_k) = -\sum_{j=1, j\neq k}^{\mathscr{N}_{\mathscr{X}}} (\mathscr{X}_k - \mathscr{X}_j), \mathfrak{F}or\ k = 1,2,3,\ldots,\mathscr{N}_{\mathscr{X}} \tag{27}$$

4.2. Two-dimensional approximation

Using the DQA's principles, the first and second derivatives of a function such as $\mathscr{G}(\mathscr{X},\mathscr{Y})$ may be produced as follows [54]:

$$\left.\frac{\partial \mathscr{T}}{\partial \mathscr{X}}\right|_{\mathscr{X}=\mathscr{X}_s, \mathscr{Y}=\mathscr{Y}_j} = \sum_{p=1}^{\mathscr{N}_{\mathscr{X}}}\sum_{k=1}^{\mathscr{N}_{\mathscr{Y}}} \Re_{sp}^{\mathscr{X}} \mathfrak{i}_{pk}^{\mathscr{Y}} \mathscr{T}_{kj} \tag{28}$$

$$\left.\frac{\partial \mathscr{T}}{\partial \mathscr{Y}}\right|_{\mathscr{X}=\mathscr{X}_s, \mathscr{Y}=\mathscr{Y}_j} = \sum_{p=1}^{\mathscr{N}_{\mathscr{X}}}\sum_{k=1}^{\mathscr{N}_{\mathscr{Y}}} \mathfrak{i}_{sp}^{\mathscr{X}} \Re_{pk}^{\mathscr{Y}} \mathscr{T}_{kj}$$

$$\frac{\partial}{\partial \mathscr{X}}\left(\left.\frac{\partial \mathscr{T}}{\partial \mathscr{Y}}\right|_{\mathscr{X}=\mathscr{X}_s, \mathscr{Y}=\mathscr{Y}_j}\right) = \sum_{p=1}^{\mathscr{N}_{\mathscr{X}}}\sum_{k=1}^{\mathscr{N}_{\mathscr{Y}}} \Re_{sp}^{\mathscr{X}} \Re_{pk}^{\mathscr{Y}} \mathscr{T}_{kj}$$

$$\left.\frac{\partial^2 \mathscr{T}}{\partial \mathscr{X}^2}\right|_{\mathscr{X}=\mathscr{X}_s, \mathscr{Y}=\mathscr{Y}_j} = \sum_{p=1}^{\mathscr{N}_{\mathscr{X}}}\sum_{k=1}^{\mathscr{N}_{\mathscr{Y}}} \mathfrak{L}_{sp}^{\mathscr{X}} \mathfrak{i}_{pk}^{\mathscr{Y}} \mathscr{T}_{kj}$$

$$\left.\frac{\partial^2 \mathscr{T}}{\partial \mathscr{Y}^2}\right|_{\mathscr{X}=\mathscr{X}_s, \mathscr{Y}=\mathscr{Y}_j} = \sum_{p=1}^{\mathscr{N}_{\mathscr{X}}}\sum_{k=1}^{\mathscr{N}_{\mathscr{Y}}} \mathfrak{i}_{sp}^{\mathscr{X}} \mathfrak{L}_{pk}^{\mathscr{Y}} \mathscr{T}_{kj}$$

The equivalent weight coefficients are $\Re_{pk}^{\mathscr{Y}}$, $\Re_{ip}^{\mathscr{X}}$, $\mathfrak{L}_{pk}^{\mathscr{Y}}$, and $\mathfrak{L}_{ip}^{\mathscr{X}}$ in this case. Additionally, the number of discrete grid points in the circumferential and radial directions is represented by $\mathscr{N}_{\mathscr{X}}$ and $\mathscr{N}_{\mathscr{Y}}$. $\mathfrak{i}_{ip}^{\mathscr{X}}$, $\mathfrak{i}_{pk}^{\mathscr{Y}}$, $\mathfrak{i}_{ip}^{\mathscr{X}}$, and $\mathfrak{i}_{pk}^{\mathscr{Y}}$ are identity tensors, one should conclude. The polar coordination of $(\mathscr{X}_i, \mathscr{Y}_j)$ as the grid-point representation may be established as follows with the use of the Chebyshev-Gauss-Lobatto function [53]:

$$\mathscr{X}_s = \frac{a}{2}\left(1 - \cos\left(\frac{(s-1)}{(\mathscr{N}_{\mathscr{X}} - 1)}\pi\right)\right) s = 1,2,3,\ldots,\mathscr{N}_{\mathscr{X}} \tag{29}$$

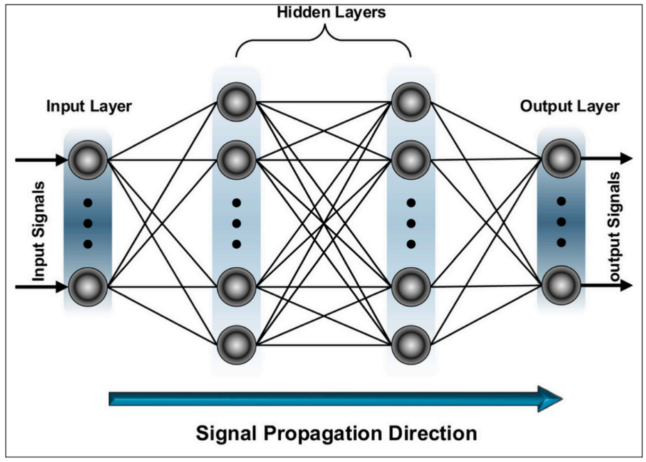

Fig. 2. A schematic view of the presented hybrid deep feedforward neural networks.

$$\mathcal{Y}_j = \frac{b}{2}\left(1-\cos\left(\frac{(j-1)}{(\mathcal{N}_y-1)}\pi\right)\right) j = 1,2,3,\dots,\mathcal{N}_y$$

The first five equations of motion (19), taking into account Eq. (28), and taking into consideration Eqs. (20) and (21) may be expressed in the following way.

$$\begin{aligned}&[\mathcal{M}^{\Delta\Delta}]_{5\mathcal{N}_x\mathcal{N}_y\times 5\mathcal{N}_x\mathcal{N}_y}\left\{\ddot{\mathfrak{Y}}\right\}_{5\mathcal{N}_x\mathcal{N}_y\times 1}\\&+[\mathcal{K}^{\mathfrak{Y}\mathfrak{Y}}]_{5\mathcal{N}_x\mathcal{N}_y\times 5\mathcal{N}_x\mathcal{N}_y}\{\mathfrak{Y}\}_{5\mathcal{N}_x\mathcal{N}_y\times 1}\\&+[\mathcal{K}^{\mathfrak{Y}\Phi}]_{5\mathcal{N}_x\mathcal{N}_y\times 2\mathcal{N}_x\mathcal{N}_y}\{\mathfrak{X}\}_{2\mathcal{N}_x\mathcal{N}_y\times 1}\\&=\{\mathcal{F}^{\mathfrak{Y}}\}_{5\mathcal{N}_x\mathcal{N}_y\times 1}\end{aligned} \tag{30}$$

Here, $\{\mathfrak{Y}\} = \{\mathcal{U}_0, \mathcal{V}_0, \mathcal{W}_0, \mathcal{f}_x, \mathcal{f}_y\}^T$ is the displacement vector and $\{\mathfrak{X}\} = \{\mathcal{A},\mathcal{S}\}^T$ is the electrical potential vector. Additionally, the mass, stiffness, and piezoelectric matrices are represented by the matrices $[\mathcal{M}^{\mathfrak{Y}\mathfrak{Y}}]$, $[\mathcal{K}^{\mathfrak{Y}\mathfrak{Y}}]$ and $[\mathcal{K}^{\mathfrak{Y}\mathfrak{X}}]$, respectively. These matrices' components are listed in Appendix A. Additionally, the term $[\mathcal{C}^{\mathfrak{Y}\mathfrak{Y}}] = (\alpha[\mathcal{M}^{\mathfrak{Y}\mathfrak{Y}}]+\beta[\mathcal{K}^{\mathfrak{Y}\mathfrak{Y}}])\{\dot{\mathfrak{Y}}\}_{5\mathcal{N}_x\mathcal{N}_y\times 1}$ should be added to the left side of the preceding equation if Rayleigh damping is of relevance. In this case, α and β are Rayleigh constants [52]. Electrical equations, represented as the sixth and seventh equations of the system, may be expressed similarly to mechanical equations by taking into account Eqs. (20), and (21)

$$\begin{aligned}&[\mathcal{K}^{\mathfrak{X}\mathfrak{Y}}]_{2\mathcal{N}_x\mathcal{N}_y\times 5\mathcal{N}_x\mathcal{N}_y}\{\mathfrak{Y}\}_{5\mathcal{N}_x\mathcal{N}_y\times 1}\\&-[\mathcal{K}^{\mathfrak{X}\mathfrak{X}}]_{2\mathcal{N}_x\mathcal{N}_y\times 2\mathcal{N}_x\mathcal{N}_y}\{\mathfrak{X}\}_{2\mathcal{N}_x\mathcal{N}_y\times 1}\\&=\{\mathcal{F}^{\mathfrak{X}}\}_{2\mathcal{N}_x\mathcal{N}_y\times 1}\end{aligned} \tag{31}$$

Here, $[\mathcal{K}^{\mathfrak{X}\mathfrak{Y}}] = [\mathcal{K}^{\mathfrak{X}\mathfrak{Y}}]^T$ and $[\mathcal{K}^{\mathfrak{X}\mathfrak{X}}]$ is the permittivity matrix that its elements are presented in Appendix A.

When $\{\mathfrak{X}\}$ is eliminated between Eqs. (30), (31), displacement vector is revealed through the next system of equations

When there is no controller scheme between the piezoelectric layers, the following equation is achieved (i.e., passive case). In this instance, $\mathcal{F}^{\mathfrak{X}}$ equals zero if both piezoelectric layers function as sensors; however, $\mathcal{F}^{\mathfrak{X}} \neq 0$ if they function as actuators. If piezoelectric layers serve as the sensor in this scenario, the sensory voltage is determined using Eq. (31) as

$$\{\mathfrak{X}\} = [\mathcal{K}^{\mathfrak{X}\mathfrak{X}}]^{-1}_{2\mathcal{N}_x\mathcal{N}_y\times 2\mathcal{N}_x\mathcal{N}_y}[\mathcal{K}^{\mathfrak{X}\mathfrak{Y}}]_{2\mathcal{N}_x\mathcal{N}_y\times 5\mathcal{N}_x\mathcal{N}_y}\{\mathfrak{Y}\}_{5\mathcal{N}_x\mathcal{N}_y\times 1} \tag{33}$$

When the controller rule (22) is created between piezoelectric layers (i.e., the active case [55]), one layer acts as the sensor (the bottom layer) and the other as the actuator (the top layer). The mechanical stimulation of the panel results in the generation and accumulation of electric charges in the sensor layer. Through the closed-loop regulation described in Eq. (22), the charges produce electric potentials that are amplified and converted into the open circuit voltage.

The distributed actuator then receives the signal again. Stresses and strains are produced as a result of the piezoelectric layer effect, which was noted in the sixth equation of Eq. (19). The resulting force has the ability to actively regulate the structure's dynamic response. The produced potential on the sensor is obtained from Eq. (19) because the sensor layer does not take any applied external charge into account as an input.

$$\{\mathcal{S}\} = [\mathcal{K}^{\mathfrak{X}\mathfrak{X}}]^{-1^s}_{1\times 1}[\mathcal{K}^{\mathfrak{X}\mathfrak{Y}}]^s_{1\times 5\mathcal{N}_x\mathcal{N}_y}\{\mathfrak{Y}\}_{5\mathcal{N}_x\mathcal{N}_y\times 1} \tag{34}$$

Taking into account the specification of the controller law (Eq. (22)) the actuation voltage is found as

$$\{\mathcal{A}\} = -G_{\mathcal{V}}[\mathcal{K}^{\mathfrak{X}\mathfrak{X}}]^{-1^s}_{1\times 1}[\mathcal{K}^{\mathfrak{X}\mathfrak{Y}}]^s_{1\times 5\mathcal{N}_x\mathcal{N}_y}\{\dot{\mathfrak{Y}}\}_{5\mathcal{N}_x\mathcal{N}_y\times 1} \tag{35}$$

Combining the Eqs. (30), (34), (35) gives us

$$\begin{aligned}&[\mathcal{M}^{\mathfrak{Y}\mathfrak{Y}}]_{5\mathcal{N}_x\mathcal{N}_y\times 5\mathcal{N}_x\mathcal{N}_y}\left\{\ddot{\mathfrak{Y}}\right\}_{5\mathcal{N}_x\mathcal{N}_y\times 1}+[\mathcal{C}^{\mathfrak{Y}\mathfrak{Y}}]_{5\mathcal{N}_x\mathcal{N}_y\times 5\mathcal{N}_x\mathcal{N}_y}\{\dot{\mathfrak{Y}}\}_{5\mathcal{N}_x\mathcal{N}_y\times 1}\\&+\left([\mathcal{K}^{\mathfrak{Y}\mathfrak{Y}}]_{5\mathcal{N}_x\mathcal{N}_y\times 5\mathcal{N}_x\mathcal{N}_y}+[\mathcal{K}^{\mathfrak{Y}\mathfrak{X}}]_{5\mathcal{N}_x\mathcal{N}_y\times 2\mathcal{N}_x\mathcal{N}_y}[\mathcal{K}^{\mathfrak{X}\mathfrak{X}}]^{-1}_{2\mathcal{N}_x\mathcal{N}_y\times 2\mathcal{N}_x\mathcal{N}_y}[\mathcal{K}^{\mathfrak{X}\mathfrak{Y}}]_{2\mathcal{N}_x\mathcal{N}_y\times 5\mathcal{N}_x\mathcal{N}_y}\right)\{\mathfrak{Y}\}_{5\mathcal{N}_x\mathcal{N}_y\times 1}\\&=\{\mathcal{F}^{\mathfrak{Y}}_{mn}\}_{5\mathcal{N}_x\mathcal{N}_y\times 1}+[\mathcal{K}^{\mathfrak{Y}\mathfrak{X}}]_{5\mathcal{N}_x\mathcal{N}_y\times 2\mathcal{N}_x\mathcal{N}_y}[\mathcal{K}^{\mathfrak{X}\mathfrak{X}}]^{-1}_{2\mathcal{N}_x\mathcal{N}_y\times 2\mathcal{N}_x\mathcal{N}_y}\{\mathcal{F}^{\mathfrak{X}}\}_{2\mathcal{N}_x\mathcal{N}_y\times 1}\end{aligned} \tag{32}$$

```
rmse_ann = sqrt(mean((y_pred_ann - y_test).^2));
rmse_svr = sqrt(mean((y_pred_svr - y_test).^2));
rmse_hybrid = sqrt(mean((y_pred_hybrid - y_test).^2));
```

$$[\widetilde{\mathscr{M}}]_{5\mathscr{N}_x\mathscr{N}_y\times 5\mathscr{N}_x\mathscr{N}_y}\left\{\ddot{\mathfrak{Y}}\right\}_{5\mathscr{N}_x\mathscr{N}_y\times 1}+[\widetilde{\mathscr{C}}]_{5\mathscr{N}_x\mathscr{N}_y\times 5\mathscr{N}_x\mathscr{N}_y}\{\dot{\mathfrak{Y}}\}_{5\mathscr{N}_x\mathscr{N}_y\times 1}+[\widetilde{\mathscr{K}}]_{5\mathscr{N}_x\mathscr{N}_y\times 5\mathscr{N}_x\mathscr{N}_y}\{\mathfrak{Y}\}_{5\mathscr{N}_x\mathscr{N}_y\times 1}=\{\widetilde{\mathscr{F}}\}_{5\mathscr{N}_x\mathscr{N}_y\times 1}. \tag{36}$$

wherein the need for the following definitions

$$[\widetilde{\mathscr{M}}]=[\mathscr{M}^{\mathfrak{Y}\mathfrak{Y}}]_{5\mathscr{N}_x\mathscr{N}_y\times 5\mathscr{N}_x\mathscr{N}_y} \tag{37}$$

$$[\widetilde{\mathscr{C}}]=\alpha[\mathscr{M}^{\mathfrak{Y}\mathfrak{Y}}]_{5\mathscr{N}_x\mathscr{N}_y\times 5\mathscr{N}_x\mathscr{N}_y}+\beta[\mathscr{K}^{\mathfrak{Y}\mathfrak{Y}}]_{5\mathscr{N}_x\mathscr{N}_y\times 5\mathscr{N}_x\mathscr{N}_y}-G_{\mathscr{V}}[\mathscr{K}^{\mathfrak{Y}\mathfrak{X}}]^{a}_{5\mathscr{N}_x\mathscr{N}_y\times 1}[\mathscr{K}^{\mathfrak{X}\mathfrak{X}}]^{-1^s}_{1\times 1}[\mathscr{K}^{\mathfrak{X}\mathfrak{Y}}]^{s}_{1\times 5\mathscr{N}_x\mathscr{N}_y}$$

$$[\widetilde{\mathscr{K}}_{mn}]=[\mathscr{K}^{\mathfrak{Y}\mathfrak{Y}}]_{5\mathscr{N}_x\mathscr{N}_y\times 5\mathscr{N}_x\mathscr{N}_y}+[\mathscr{K}^{\mathfrak{Y}\mathfrak{X}}]^{s}_{5\mathscr{N}_x\mathscr{N}_y\times 1}[\mathscr{K}^{\mathfrak{X}\mathfrak{X}}]^{-1^s}_{1\times 1}[\mathscr{K}^{\mathfrak{X}\mathfrak{Y}}]^{s}_{1\times 5\mathscr{N}_x\mathscr{N}_y}$$

$$\{\widetilde{\mathscr{F}}\}=\{\mathscr{F}^{\mathfrak{Y}}\}_{5\mathscr{N}_x\mathscr{N}_y\times 1}$$

Eq. (36) is used to manage the vibration of panels using two curves.

4.3. Laplace transform

In the event that an out-of-plane dynamic loading is applied to a shell panel, the system of Eqs. (32) or (36) must be solved. Initial conditions throughout the panel should be specified in order to handle the dynamic analysis of the panel. The following starting conditions specify the panel's state before loading when it is initially at rest.

$$\mathscr{U}_0(0)=\mathscr{V}_0(0)=\mathscr{W}_0(0)=\mathscr{f}_{x}(0)=\mathscr{f}_{y}(0)=0 \tag{38}$$

$$\dot{\mathscr{U}}_0(0)=\dot{\mathscr{V}}_0(0)=\dot{\mathscr{W}}_0(0)=\dot{\mathscr{f}}_{x}(0)=\dot{\mathscr{f}}_{y}(0)=0$$

The Laplace domain transformation of Eqs. (32) or (36) results in the dynamic response of equations of motion. s is the Laplace transformation parameter, let's suppose. Under such circumstances, a new system of equations in which time dependence is abolished is obtained by applying the Laplace transform to either Eqs. (32) or (36) while keeping in mind the initial conditions (Eq. (38)). For example, equations in the Laplace domain for the situation of active control are expressed as

$$[\widetilde{\mathscr{K}}+s\widetilde{\mathscr{C}}+s^2\widetilde{\mathscr{M}}]_{5\mathscr{N}_x\mathscr{N}_y\times 5\mathscr{N}_x\mathscr{N}_y}\{\widetilde{\mathfrak{Y}}\}_{5\mathscr{N}_x\mathscr{N}_y\times 1}=\{\widetilde{\mathscr{F}}\}_{5\mathscr{N}_x\mathscr{N}_y\times 1} \tag{39}$$

Here, the Laplace transform function of each quantity is shown by a line above it.

Upon solving the system of Eq. (39), every component of the displacement vector may be acquired in a closed-form expression inside the Laplace domain. Re-transferring the displacement vector from the Laplace domain into the time domain requires the use of the Laplace inverse definition.

The displacement for each layer may be obtained by solving Eq. (39) layer-wise after applying the Laplace transform [56]. The stresses for each layer can then be derived by including the displacement for each layer in Eq. (9). The tension and displacements along the annular plate's transverse orientation would then be determined using Eqs. (11) and (14). Using the fully modified formulation of Dubner and Abate's solution [57], the displacements, stresses, heat flow, and temperature gradient term are temporally realized when the Laplace transform is inverted. Thus, the procedure for inverting the Laplace transform in this study is given by Eq. (40).

$$\mathscr{F}(t)=\frac{2e^{at}}{T}\left[-\frac{AptCommandmathbba_0}{2}+\sum_{k=0}^{\infty}\left(AptCommandmathbba_k cos\left(\frac{2k\pi t}{T}\right)-AptCommandmathbbb_k sin\left(\frac{2k\pi t}{T}\right)\right)\right] \tag{40}$$

where

$$AptCommandmathbba_0=Re[\mathfrak{f}(a)], AptCommandmathbba_k=Re\left[f\left(a+i\frac{2k\pi}{T}\right)\right], AptCommandmathbbb_k=Im\left[f\left(a+i\frac{2k\pi}{T}\right)\right] \tag{41}$$

$$s=a+i\frac{2k\pi}{T}, aT=5.$$

5. Hybrid machine learning method

Four models were utilized: two basic methods (Deep neural networks (DNN) and support vector regression (SVR)) and two optimized hybrid models grey Wolf optimizer-based SVR (GWO-SVR) and Particle Swarm Optimization based SVR (PSO-SVR). A schematic view of the presented hybrid deep feedforward neural networks is shown in Fig. 2.

5.1. Performance assessment

A random process was often used to split the experimental database into three subgroups, accounting for the classification of the majority of prior experiments; these subsets were called the training set, validation set, and testing sets [58,59]. The training set was used to optimize the model's parameters, e.g., weight and bias in the case of an Artificial Neural Network (ANN). Conversely, the validation set was used to assess the model's development and convergence during the training process. It was often used to adjust the hyperparameters. The testing set was used to assess the model's generalizability, or its capacity to correctly forecast a fresh set of databases after hyperparameter optimization [60,61]. The prediction performance difference was evaluated by comparing four machine learning models using absolute error, error percentage, mean absolute error (MAE), coefficient of determination (R^2), mean absolute percentage error (MAPE), root mean squared error (RMSE), and RMSE-to-observation's standard deviation ratio (RSR) [62]. These methods allowed for the quantification of the degree to which the expected value and the actual value were similar. Two of the parameters were determined by evaluating a single sample (mix proportion), and the remaining five were determined by the algorithm fitting degree of multiple subsets. Furthermore, it is possible to combine these five statistical factors into a single measuring parameter called the composite performance index (CPI) [63]. Eq. (42), where y_i' and y_i represent the expected and actual values, respectively, may be used to describe the eight parameters indicated before. P_j is the statistical parameter of the j-th parameter, and $\bar{y}$ is the average value. Using the same machine learning model, $P_{min,j}$ and $P_{max,j}$ represent the lowest and highest values

```
function rmse = svr_fitness(params, X_train, y_train, X_test, y_test)
    c = params(1);
    epsilon = params(2);
    epsilon_tol = params(3);
    svr_model = fitrsvm(X_train, y_train, 'KernelFunction', 'rbf',
'BoxConstraint', c, 'Epsilon', epsilon, 'EpsilonTolerance', epsilon_tol);
    y_pred = predict(svr_model, X_test);
    rmse = sqrt(mean((y_pred - y_test).^2));
end
```

```
rmse_pso = sqrt(mean((y_pred_pso - y_test).^2));
rmse_gwo = sqrt(mean((y_pred_gwo - y_test).^2));
```

Table 1
The properties of MHLNC [65].

Carbon (fiber)	Epoxy (matrix)	Carbon nanotube
$E_{11f}(GPa)$=233.05	v_m=0.34	$E_{cnt}(Gpa)$=640
$E_{22f}(GPa)$=23.1	ρ_m(kgm3)=1200	$d_{cnt}(m)$=0.14×10-9
$G_{11f}(GPa)$=8.96	$E_m(Gpa)$=3.51	$t_{cnt}(m)$=0.034×10-9
υ_f=0.2		$l_{cnt}(m)$=0.25×10-9
$\rho_f(kg/m^3)$=1750		ϑ12=0.33
		$\rho_{cnt}(kg/m^3)$=1350

Table 2
Properties of G−1195N as sensor and actuator layer [42].

E (GPa)	ρ (kg/m³)	ν	e₃₁ (c/m²)	e₃₂ (c/m²)	η₃ (F/m)
63	7600	0.3	22.86	22.86	1.5×10^{-8}

Table 3
Comparison of the nondimensional frequencies of the FG doubly curved shells.

	Method	$k=0$	$k=0.5$	$k=1$	$k=4$	$k=10$
$R_1=R_2\to\infty$	Ref. [67]	0.0577	0.0490	0.0442	0.0382	0.0366
	Ref. [66]	0.0577	0.0492	0.0443	0.0381	0.0364
	Present	0.0576	0.0491	0.0441	0.0382	0.0365
$R_1=R_2$	Ref. [67]	0.0746	0.0646	0.0588	0.0491	0.0455
	Ref. [66]	0.0751	0.0657	0.0600	0.0503	0.0464
	Present	0.0747	0.0645	0.0587	0.0490	0.0454
$R_1=-R_2$	Ref. [67]	0.0548	0.0465	0.0420	0.0363	0.0347
	Ref. [66]	0.0563	0.0479	0.0432	0.0372	0.0355
	Present	0.0547	0.0464	0.0422	0.0362	0.0346
$R_2\to\infty$	Ref. [67]	0.0617	0.0527	0.0477	0.0407	0.0385
	Ref. [66]	0.0622	0.0535	0.0485	0.0413	0.0390
	Present	0.0618	0.0525	0.0476	0.0407	0.0383

of the j^{th} statistical parameter for each of the five values.

$$Absoluteerror = y_i' - y_i \tag{42}$$

$$Errorpercentage = \frac{y'_i - y_i}{y_i}$$

$$R^2 = 1 - \frac{\sum_{i=1}^{n}(y'_i - y_i)^2}{\sum_{i=1}^{n}(y_i - \bar{y})^2}$$

$$RMSE = \sqrt{\frac{\sum_{i=1}^{n}(y'_i - y_i)^2}{n}}$$

$$MAE = \frac{1}{n}\sum_{i=1}^{n}|y'_i - y_i|$$

$$MAPE = \frac{1}{n}\sum_{i=1}^{n}\left|\frac{y'_i - y_i}{y_i}\right| \times 100$$

$$RSR = \frac{RMSE}{\sqrt{\frac{1}{n}\sum_{i=1}^{n}(y_i - \bar{y})^2}}$$

$$CPI = \frac{1}{N}\sum_{j=1}^{N}\frac{P_j - P_{min,j}}{P_{max,j} - P_{min,j}}$$

5.2. Partial dependence plots (PDP)

The primary goal of a machine learning business application is to generate informed assessments that can be used for making decisions. Model interpretability refers to the understanding of the model's underlying mechanism and the results it produces. The higher the interpretability of a machine learning model, the easier it is for humans to understand the reasoning behind its conclusions or predictions. The significance of this is evident in the following ways: during the modeling stage, it aids developers in understanding, comparing, selecting, and fine-tuning the model as needed; during the operational stage, it clarifies the model's internal workings to the business party and explains the model's outcomes. Machine learning (ML) is often considered a black box activity, where the link between data, calculations, and projected outcomes is not easily understood. To address this, interpretable local or global methodologies are needed to visually analyze the ML process. Partial dependence plot (PDP) is a commonly used method for global interpretability. It can not only show the limited impact of one or two features on the model's predictions but also determine the importance of features based on the operational results. The PDP analysis can determine whether the relationship between the target variable and the feature is linear, monotonous, or more complex [64]. The partial dependence function in regression is formally defined as:

$$\hat{f}_{x_S}(x_S) = E_{x_C}\left[\hat{f}_{x_S}(x_S, x_C)\right] = \int \hat{f}_{x_S}(x_S, x_C)dP(x_C) \tag{43}$$

The variable x_S represents the feature and the partial dependency function that will be depicted, whereas x_C represents the other characteristics utilized by the machine learning model. Typically, set S possesses only one or two distinct attributes. We are specifically interested in the feature (s) in S that have a significant impact on the prediction. The feature space x is defined by the concatenated feature vectors x_S and x_C. Partial dependency is a technique that involves calculating the average output of a machine learning model for a specific feature distribution in set C. This allows us to understand the relationship between the features in set C and the predicted outcomes. By disregarding or downplaying other characteristics, a function can be derived that relies

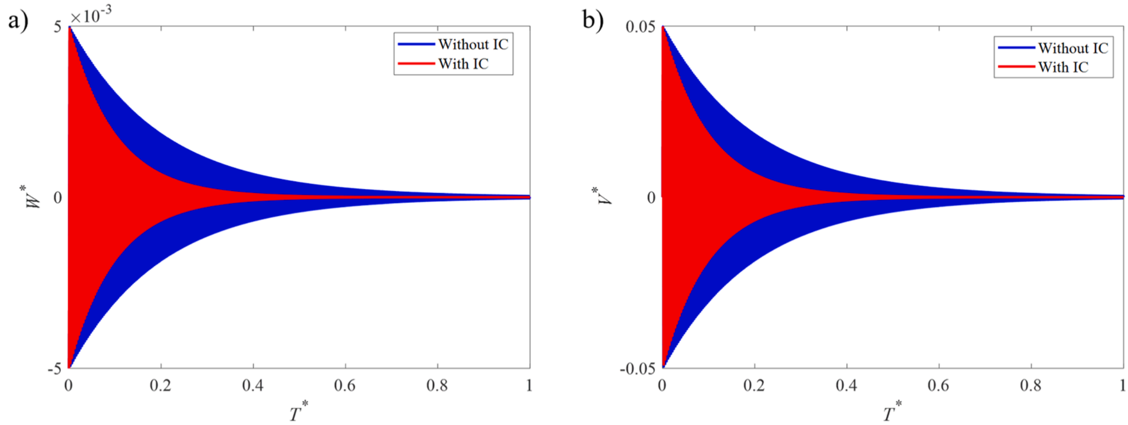

Fig. 3. Dimensionless dynamic a) deflection and b) velocity with respect to dimensionless times (T* × 1000) plots with and without an intelligence controller (IC).

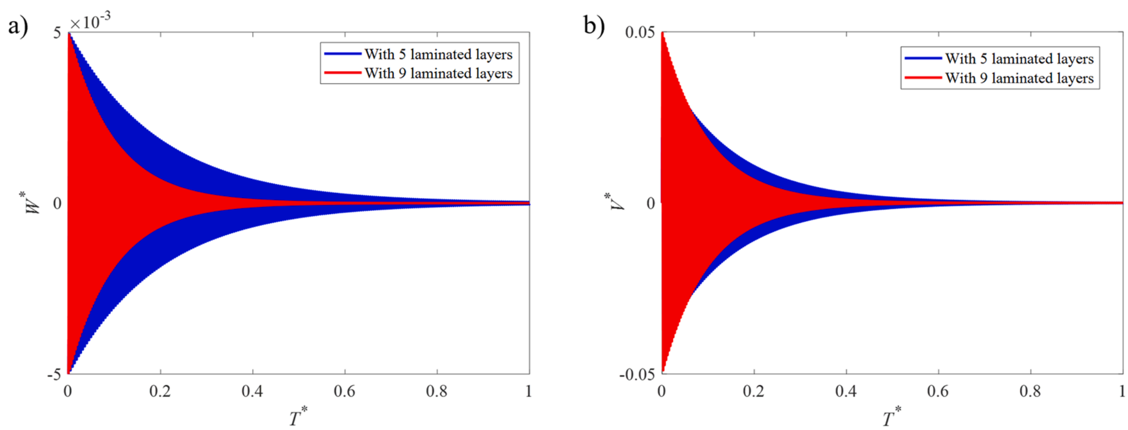

Fig. 4. Dimensionless dynamic a) deflection and b) velocity with respect to dimensionless time (T* × 1000) plots with 5 and 9 laminated layers.

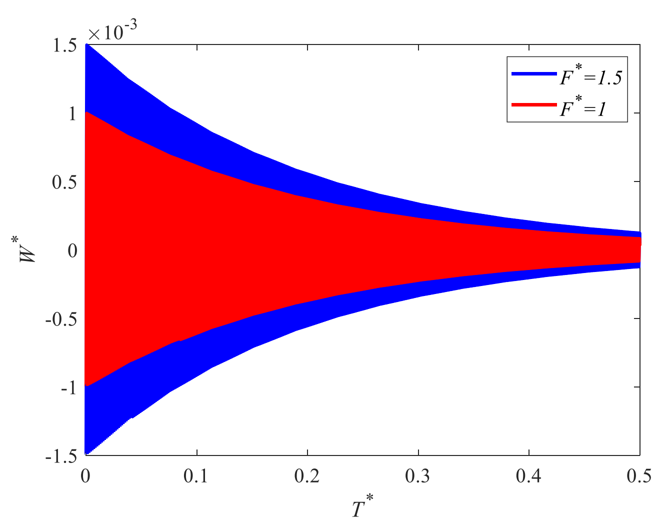

Fig. 5. Dimensionless dynamic deflection with respect to dimensionless time (T* × 1000).

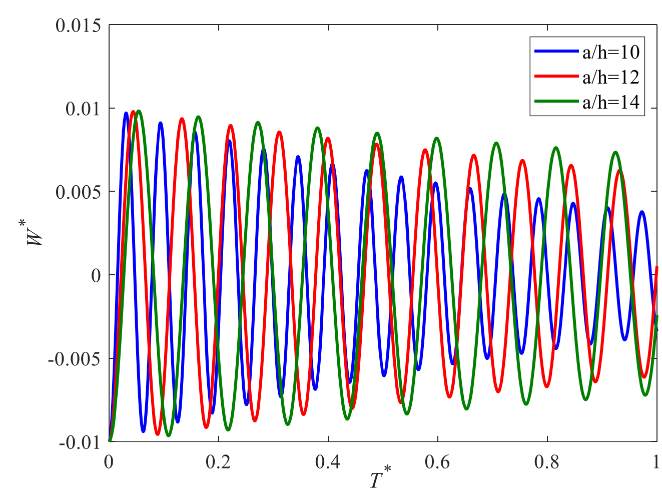

Fig. 6. Dimensionless dynamic deflection with respect to dimensionless time in different length to thickness ratio (a/h).

just on the features present in set S, including how they interact with one another. Here are various steps of the presented MATLAB code implementing a hybrid machine learning algorithm using artificial neural network (ANN) and support vector regression (SVR), along with two optimized hybrid models using Particle Swarm Optimization (PSO) and Grey Wolf Optimizer (GWO) for SVR:

Step 1: Load Data

```
load('vibrational_data.mat');
```

This step loads the data from the file 'vibrational_data.mat' into the MATLAB environment. Make sure the file contains the necessary data for training and testing.

Step 2: Data Preprocessing unnuber figure

Here, the data is split into training and testing sets. The 'train_ratio'

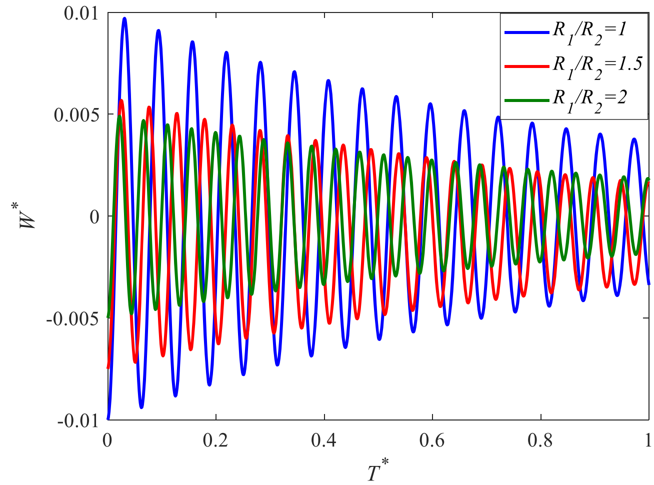

Fig. 7. Dimensionless dynamic deflection with respect to dimensionless time in different radius curvature ratios (R_1/R_2).

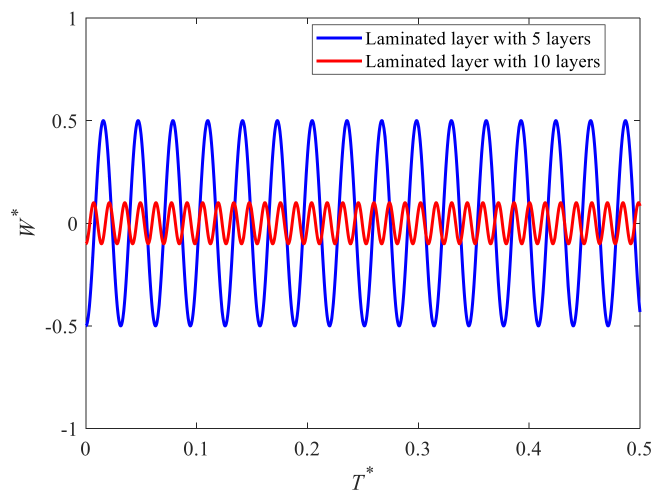

Fig. 8. Dimensionless dynamic deflection in the free vibration zone with respect to dimensionless time with 5 and 10 laminated layers.

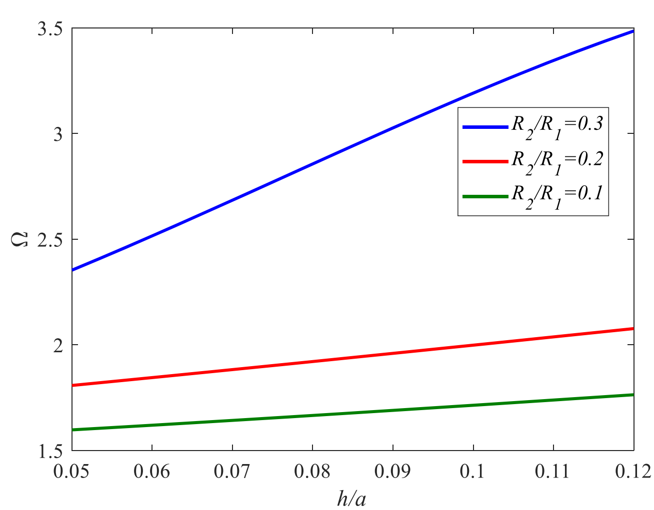

Fig. 9. Dimensionless natural frequency under external excitation with respect to h/a for different radius curvature ratios.

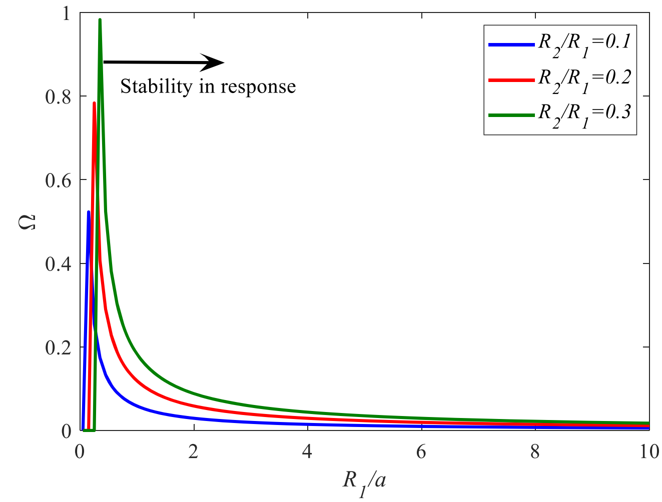

Fig. 10. Dimensionless natural frequency under external excitation with respect to R_1/a for different radius curvature ratios.

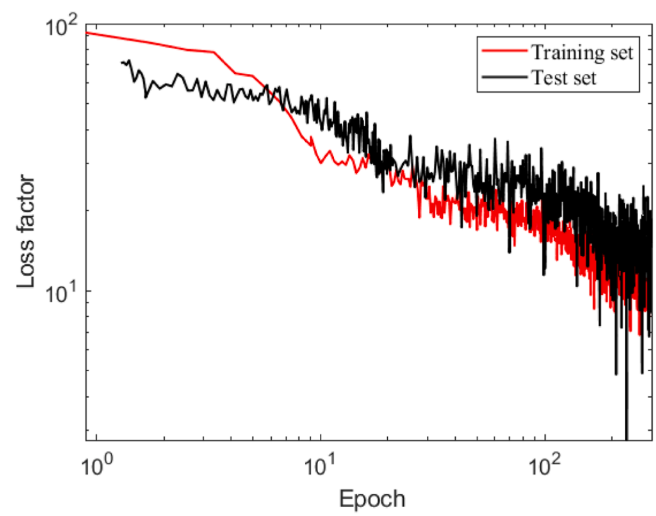

Fig. 11. Loss factor with respect to epoch for training and test sets of mathematical modeling datasets.

variable determines the proportion of data used for training. The ’train_data’ and ’test_data’ variables store the training and testing datasets, respectively.

Step 3: Feature and Target Variable Extraction unnuber figure

In this step, the features (X) and target variables (y) are extracted from the training and testing datasets. ’X_train’ and ’X_test’ contain the features, while ’y_train’ and ’y_test’ contain the corresponding target values.

Step 4: Training the Artificial Neural Network (ANN)

```
hidden_layer_size = 10;
net = fitnet(hidden_layer_size);
net = train(net, X_train’, y_train’);
```

An ANN model is trained using the ’fitnet’ function with a specified number of neurons in the hidden layer (’hidden_layer_size’). The ’train’ function is then used to train the network with the training data.

Step 5: Prediction using ANN

```
y_pred_ann = net(X_test’)’;
```

The trained ANN model is used to make predictions on the testing data (’X_test’). The predictions are stored in ’y_pred_ann’.

Step 6: Training the Support Vector Regression (SVR) Model

```
svr_model = fitrsvm(X_train, y_train);
```

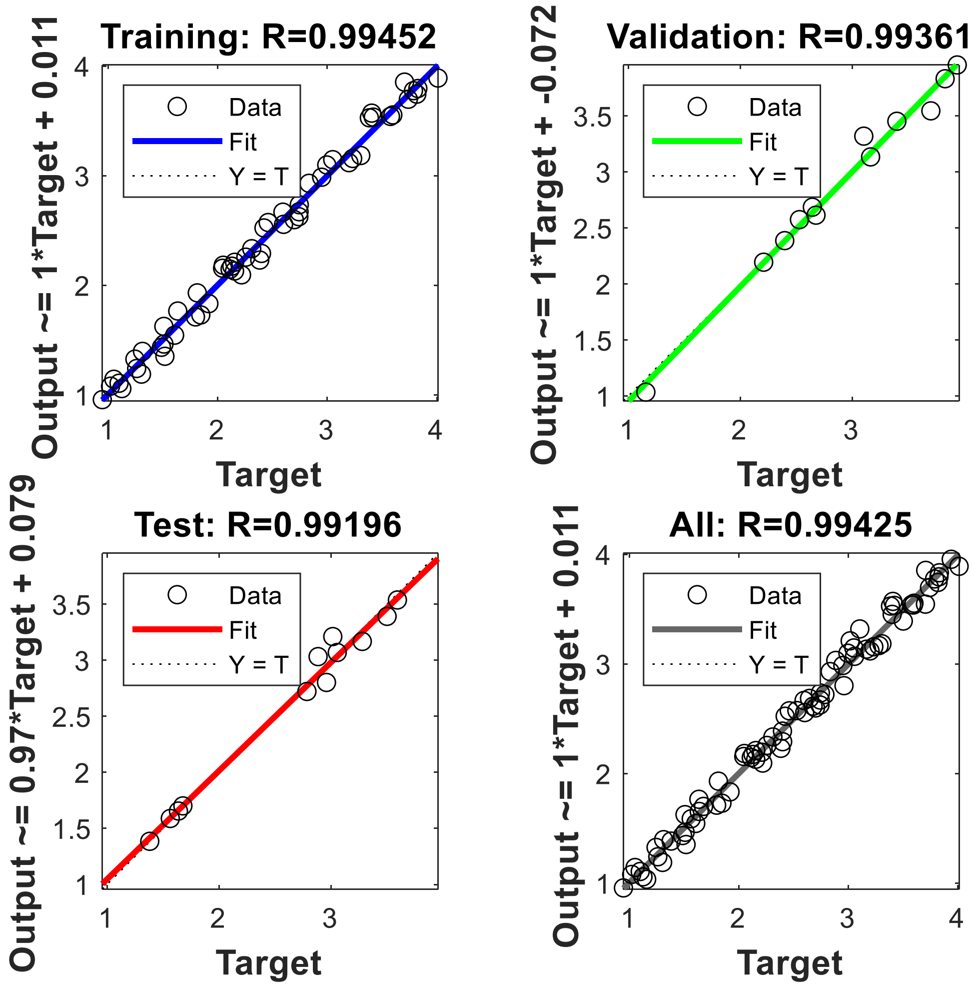

Fig. 12. Output-Target and R-value plots for training and test sets of mathematical modeling datasets.

The trained SVR model is used to make predictions on the testing data ('X_test'). The predictions are stored in 'y_pred_svr'.

Step 8: Combining Predictions from ANN and SVR

`y_pred_hybrid = (y_pred_ann + y_pred_svr) / 2;`

The predictions from the ANN and SVR models are combined by taking their average. This creates a hybrid prediction ('y_pred_hybrid').

Step 9: Evaluation

Root Mean Square Error (RMSE) is calculated for each model to evaluate their performance on the testing data.

Step 10: Optimization using Particle Swarm Optimization (PSO)

`options = optimoptions(@particleswarm, 'SwarmSize', 50, 'MaxIterations', 100);`

`pso_params = particleswarm(@(params) svr_fitness (params, X_train, y_train, X_test, y_test), 3, [], [], [], [], [0 0 0], [10 10 10], options);`

PSO is used to optimize the SVR parameters (BoxConstraint, Epsilon, and EpsilonTolerance) by minimizing the fitness function 'svr_fitness'.

Step 11: Optimization using Grey Wolf Optimizer (GWO)

`options_gwo = optimoptions(@ga, 'MaxGenerations', 100);`

`gwo_params = ga(@(params) svr_fitness(params, X_train, y_train, X_test, y_test), 3, [], [], [], [], [0 0 0], [10 10 10], options_gwo);`

GWO is used to optimize the SVR parameters (BoxConstraint, Epsilon, and EpsilonTolerance) by minimizing the fitness function 'svr_fitness'.

Step 12: Defining Fitness Function

This function calculates the RMSE of the SVR model with given parameters ('params') on the testing data.

Step 13: Prediction using PSO-SVR and GWO-SVR y_pred_pso = predict(svr_model_pso, X_test); y_pred_gwo = predict(svr_model_gwo, X_test);

The optimized SVR models obtained from PSO and GWO are used to make predictions on the testing data.

Step 14: Evaluation of PSO-SVR and GWO-SVR

RMSE is calculated for the predictions made by PSO-SVR and GWO-SVR to evaluate their performance on the testing data. This summarizes the various steps involved in the provided MATLAB code for a hybrid machine learning algorithm integrating ANN and SVR, along with PSO and GWO optimization techniques for SVR.

6. Results and Discussion

In this part, the influence of various parameters on the intelligent controller for mitigating vibrations induced by external shock on the presented sandwich structure. Tables 1 and 2 show the material properties of the core layer (MHLNC) and face sheets (G − 1195N as sensor and actuator layer), respectively.

In this section, using the presented hybrid machine learning algorithm, and mathematical modeling of the controller system, an intelligent controller (IC) is presented to control the caused fluctuation in the sandwich doubly curved panel under external excitation. Now, in this section, the effects of various parameters in IC of the sandwich doubly curved panel used external excitation is presented in detail.

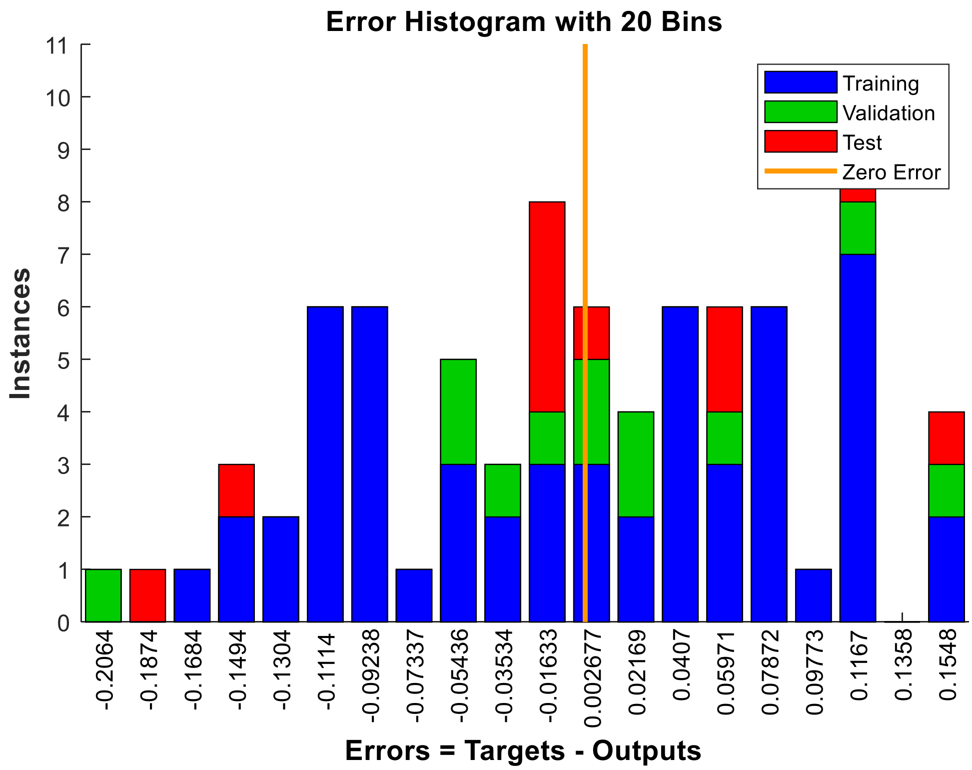

Fig. 13. Error histogram of the training and test sets of mathematical modeling datasets.

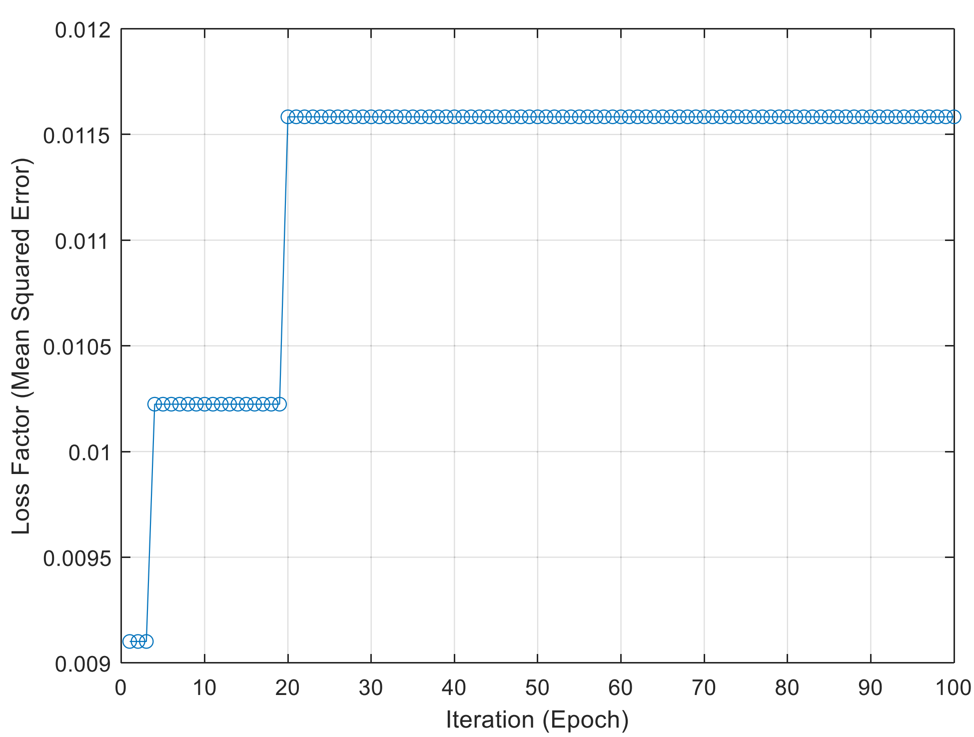

Fig. 14. Mean squared error (MSE) of the results for various iterations.

6.1. *Verification study*

To show the accuracy of the mathematical modeling and solution procedure section of the presented work, the results of the presented doubly curved panel by changing the material properties to the one functionally graded (FG) layer are compared with the outcomes of Refs. [66,67] in Table 3. As is seen, the results are compared to obtain the eigenvalue parameter of the solution procedure for various curvature factors and FG power index. As is seen, by increasing the FG power index, the dimensionless frequency of the mentioned structure due to decreasing the stiffness, decreases. Also, an increase in the curvature factors results in an increase in the dimensionless frequency of the

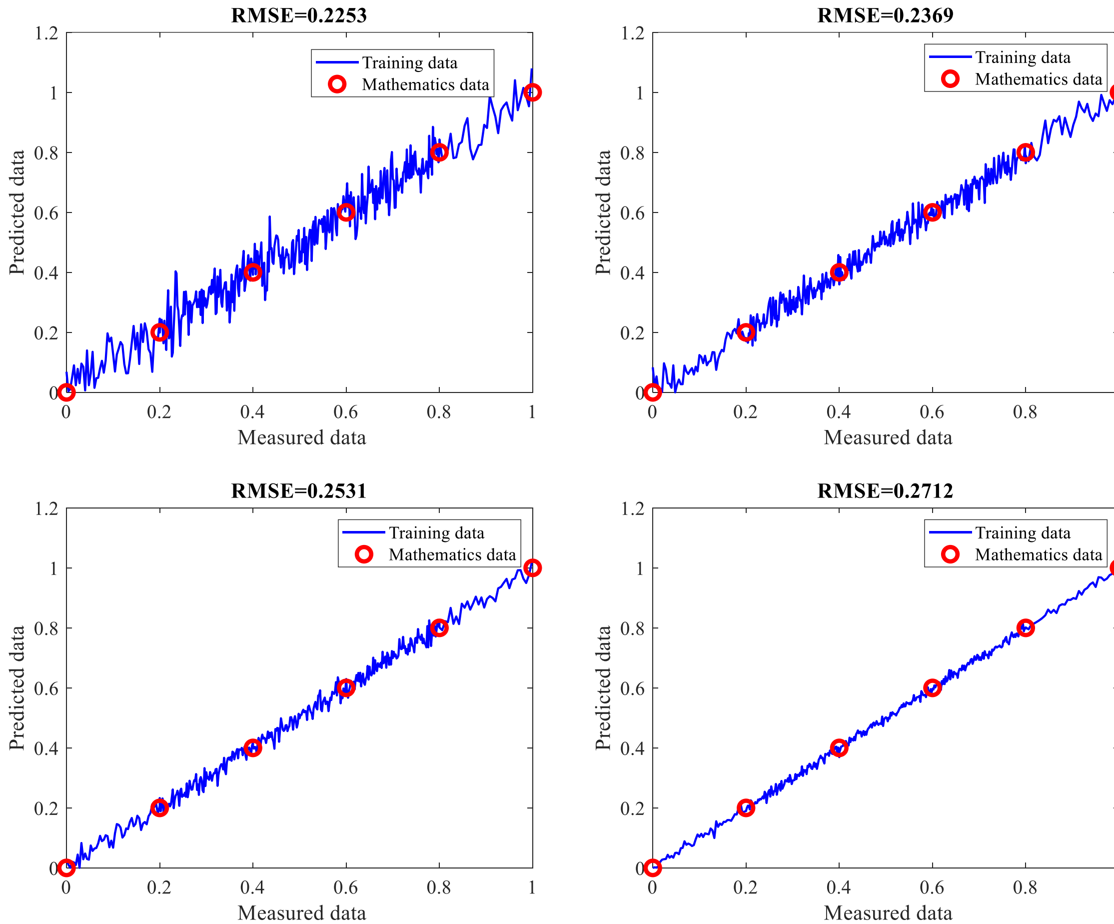

Fig. 15. Prediction data with respect to measured data of training and mathematics data for various RMSE parameters.

system. It can be concluded that the results of the current work are in good agreement with the outcomes of other published articles (Refs. [66, 67]).

6.2. Parameter study

6.2.1. Applied controller study

The image consists of two plots, labeled (a) and (b), illustrating the behavior of a system under the influence of an intelligent controller (IC) over a dimensionless time parameter (T*). In plot (a), the horizontal axis represents (T*), ranging from 0 to 1, while the vertical axis is labeled as the dimensionless deflection (W*), spanning from approximately -5 to 5. This plot shows two datasets: one labeled "Without IC" in blue and the other "With IC" in red. The blue-shaded region indicates the variance for the "Without IC" scenario, while the red-shaded region represents the variance for the "With IC" scenario. Initially, the deflection in the "Without IC" case shows larger absolute values compared to the "With IC" case. As T* increases towards 1, both datasets converge towards zero, with the "With IC" dataset displaying slightly less variance than the "Without IC" dataset, indicating that the intelligent controller effectively reduces the deflection over time. In plot (b), the horizontal axis again denotes (T*), ranging from 0 to 1, and the vertical axis is labeled as the dimensionless velocity (V*), with a range from approximately -0.05 to 0.05. This plot also features two datasets: "Without IC" in blue and "With IC" in red. Both datasets exhibit similar convergence behavior towards zero as T* approaches 1. The blue region, representing the "Without IC" data, initially shows a broader distribution, indicating greater variation in velocity compared to the red region ("With IC"). This suggests that the intelligent controller helps in stabilizing the velocity more effectively than without its use. Overall, these plots illustrate the impact of using an intelligent controller on the dimensionless deflection and velocity of a system as functions of T*. The convergence towards zero in both cases implies that the influence of the intelligent controller leads to more stable and reduced deflection and velocity over time. The shaded areas depict the spread or variance of the data, highlighting how the intelligent controller affects the variability and stability of the system throughout the observed time frame. These plots likely originate from a study analyzing the effectiveness of intelligent controllers in managing dynamic or physical processes. Analyzing the laminated composite doubly curved panel under external excitation resulted in fluctuations and vibrations. By connecting this composite panel to a controller with a sensor-actuator system, the vibrations were dampened. Fig. 3 illustrates the dimensionless dynamic parameters of the panel under forced external excitation with and without an intelligent controller (IC). In which, the dynamic parameters were calculated for the tip of the beam where the most bending and movement occurred.

It can be seen that with the IC, both parameters of W^* and V^* stabilized quite rapidly. Continuingly, since the structure under study was a layered composite panel, this evaluation was also carried out for the composite having various numbers of layers of 5 and 9 (Fig. 4).

Fig. 5 demonstrates the effect of increased cross-section area in the composite panels. Whereas, it affects the tip deflection more than the velocity. Structurally speaking, when the cross-section area of a shell-like structure increases in height with a constant width, the second moment of area rises. This phenomenon enhances the stiffness of the overall structure. Therefore, less deflection, less velocity, as well as lower vibration, is concluded in bending. Further evaluating the composite panel, the dimensionless external dynamic force (F^*) with values of 1 and 1.5 was applied. The results are presented in Fig. 5.

The plot demonstrates the direct relationship between the bending

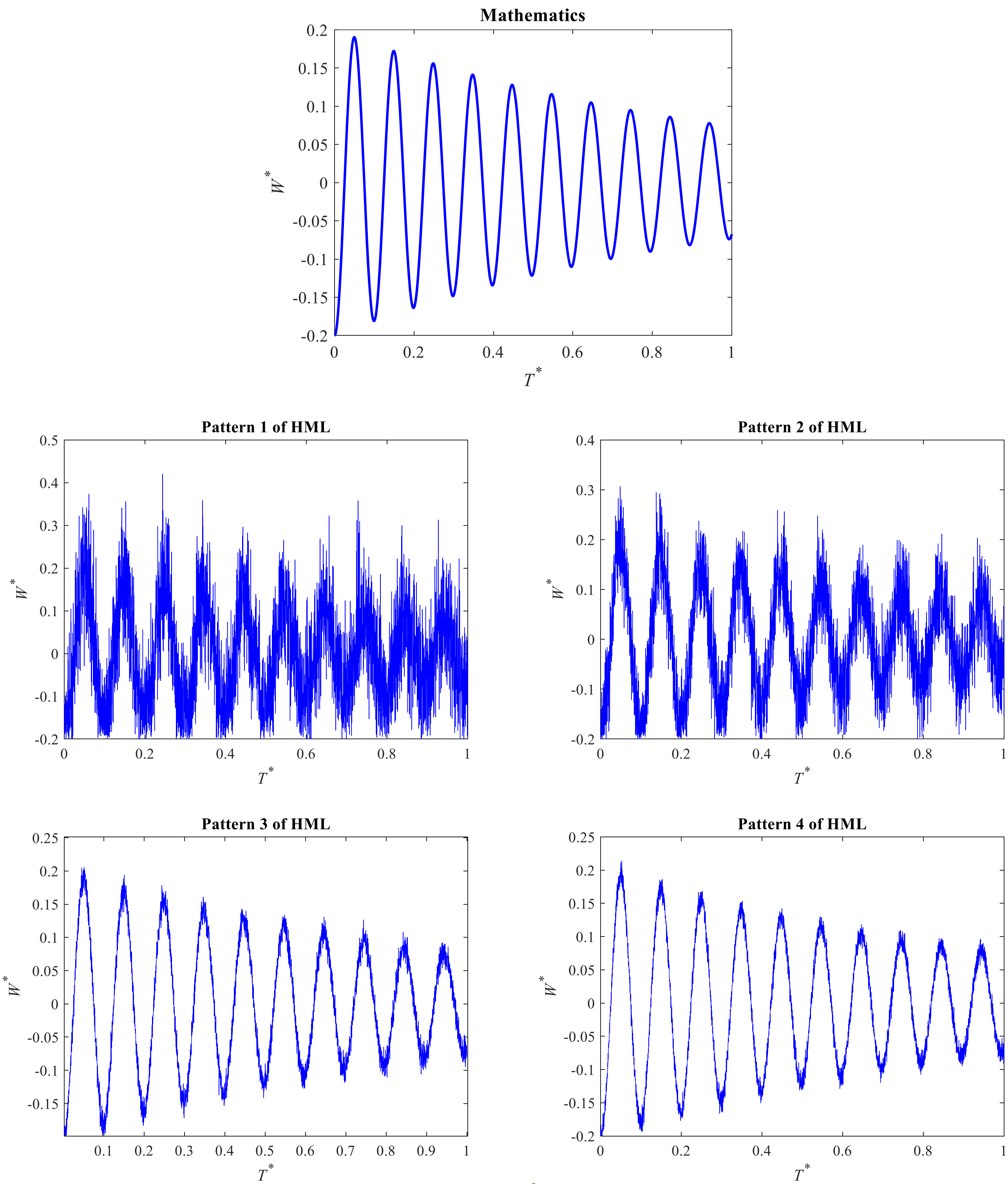

Fig. 16. Predicted and measured dimensionless deflection with respect to dimensionless time for different HML patterns.

force and the resulting deflection. That is, by increasing the excitation force, the bending moment rises and thus, the composite panel deflects more. To further investigate the dimensionless dynamic deflection of the beam under external excitation, the length-to-thickness ratio of the doubly curved panel (a/h) was studied with respect to dimensionless time in the range between 0 and 1 as presented in Fig. 6. Additionally, the ratio of the radius curvature factors along x and y directions were considered for evaluation as the radius curvature ratio, accordingly (R_1/R_2). Fig. 7 depicts the plotted curves for this ratio equal to 1, 1.5, and 2, respectively.

Both of the defined ratios show the dimensionless dynamic deflection moving towards stability. However, the speed of reaching this condition varies between the values. As the length-to-thickness ratio increases, the structure seems to become less stable. On the contrary, the largest radius curvature ratio of 2 provides the most stable condition among the radius curvature ratios.

6.2.2. Natural frequency study

Apart from varying amplitudes, the natural frequency was also evaluated for the laminated composite doubly curved panel under external excitation. Fig. 8 shows the natural frequency results for 5 and 10-layered laminated composite panels. It is observed that similar to the aforementioned results, the more layers the composite has, the lower the dimensionless dynamic deflection is.

In addition to studying multiple layers, radius curvature radius was also examined. The results given in Fig. 9 indicate that lower values of R_2/R_1 result in lower natural frequency amplitudes. The findings are in accordance with the results given in Fig. 9 whereas higher R_1/R_2 demonstrated stability sooner.

Moreover, since Ω is shown with respect to thickness to length ratio of the composite panel, all three curves demonstrate an inclining manner as the result of the thickness increasing. When the panel gets thicker, either by adding more layers or varying the thickness of each layer comprising the composite, the structure becomes more prone to stability and protests external excitations. Furthermore, the dimensionless natural frequency data was visualized with respect to the radius curvature along the x-axis to the length of the doubly curved panel ratio (R_1/a). The results of which are illustrated in Fig. 10.

Since there is a limit to R_1/a, there isn't much parameter value range in this regard. Therefore, in this case, when the value reached approximately 0.6 the structure reached stability. The peak of each curve in Fig. 10 states this value. Correspondingly, as this radius curvature ratio increases, the natural frequency experiences elevation as well, supporting the results of this frequency with respect to R_1/a.

6.3. Hybrid deep neural networks predictor

Finally, the dynamical responses of the laminated composite doubly curved panel under external excitation were predicted with the help of machine learning. Fig. 11 shows the loss factor trends for training and test sets over epochs. The red line represents the training set, and the black line represents the test set. Analyzing these trends can provide insights into the machine learning model's generalization ability across different datasets or operational conditions.

The results of Fig. 11 indicate that as the epoch increases, the loss factor shows more fluctuations for both datasets. Unlike the test set showing fluctuations from the very beginning, the training set behaves linearly until the epoch is equal to 2. The test set experiences more fluctuations and loss factor decline compared to the training set. Finally, when the epoch reached 150, the results for both training and test sets reached an equal value. To additionally examine the training and test sets, the alteration of the determined coefficient was considered as can be seen in Fig. 12.

As the determined coefficient, R was higher in value, the more the results of training and test sets were aligned with one another. This showed acceptable and good prediction of the mathematical modeling datasets. The errors of the targets and outputs are displayed in Fig. 13 considering training, test, and validation datasets as well as the zero error line.

The epoch iteration was also evaluated by the mean square error (MSE) which is shown in Fig. 14. The results demonstrate the convergence of the model at 25 iterations. Therefore, it can be concluded that 25 is the minimum number of iterations required to reach stability.

For studying the prediction and measured data, the root mean squared error (RMSE) was applied with different values (Fig. 15).

The data presented more fluctuation in the measured data between 0.2 to 0.8. Moreover, the fluctuations and noise of the training data decreased by increasing the RMSE. At RMSE equal to 0.2712, the training and mathematics data were in good accordance with each other. To validate the data, the mathematics and machine learning performed were compared. In this regard, four different patterns of hybrid machine learning (HML) algorithms were considered. The curves are presented in Fig. 16 for dimensionless dynamic deflection with respect to dimensionless time.

The data of Pattern 4 demonstrated a good correlation with the mathematics data. Thus, with the aid of artificial intelligence, good results were obtained for modeling the laminated composite doubly curved panel under external excitation.

7. Conclusion

This research introduces an intelligent controller designed to mitigate vibrations induced by external shock on composite structures. Leveraging the first-order shear deformation panel theory, a sophisticated controller scheme is devised, integrating the differential quadrature approach and Laplace transform methodologies. Moreover, ANN and SVR techniques are incorporated to enhance prediction accuracy and control efficiency. Additionally, two optimized hybrid models are proposed, integrating PSO and GWO algorithms, to further refine the controller's performance. By leveraging sophisticated control strategies and optimization algorithms, the controller can adapt dynamically to varying shock scenarios, thereby minimizing vibrations and ensuring structural integrity. Furthermore, the integration of ANN and SVR techniques enhances the controller's predictive capabilities, enabling it to anticipate and respond to dynamic changes in external shock conditions with precision. The optimized hybrid models, incorporating PSO and GWO algorithms, further refine the controller's performance, ensuring optimal control efficiency. Overall, the proposed approach represents a significant advancement in the field of structural control, with potential applications in the aerospace, automotive, and civil engineering industries. By effectively mitigating vibrations induced by external shock, this research contributes to enhancing the safety, reliability, and performance of composite structures in various engineering applications.

CRediT authorship contribution statement

Qian Zhang: Investigation, Resources, Software, Validation, Visualization, Writing – review & editing. **Shaoyong Han:** Writing – review & editing, Writing – original draft, Validation, Supervision, Software, Resources, Investigation. **Mohammed A. El-Meligy:** Resources, Software, Validation, Visualization, Writing – review & editing. **Mehdi Tlija:** Resources, Software, Validation, Writing – review & editing.

Declaration of competing interest

The authors declare that they have no conflict of interest.

Data availability

Data will be made available on request.

Funding

The scientific research projects of Wenzhou University of Technology under Grant ky202304. The laboratory opening projects of Wenzhou University of Technology under Grant WLKF24007. The authors extend their appreciation to King Saud University for funding this work through Researchers Supporting Project number (RSPD2024R685), King Saud University, Riyadh, Saudi Arabia.

Appendix A

A.1. Elements of the mass matrix

$$\mathscr{M}_{11} = -\left(\mathscr{S}_1 + 2\frac{\mathscr{S}_2}{R_1}\right)\sum_{p=1}^{\mathscr{N}_\mathscr{X}}\sum_{k=1}^{\mathscr{N}_\mathscr{Y}} \mathbb{i}_{sp}^{\mathscr{X}}\mathbb{i}_{pk}^{\mathscr{Y}}\mathscr{U}_{kj}$$

$$\mathscr{M}_{14} = -\left(\mathscr{S}_2 + \frac{\mathscr{S}_3}{R_1}\right)\sum_{p=1}^{\mathscr{N}_\mathscr{X}}\sum_{k=1}^{\mathscr{N}_\mathscr{Y}} \mathbb{i}_{sp}^{\mathscr{X}}\mathbb{i}_{pk}^{\mathscr{Y}}\mathscr{f}_{\mathscr{X}kj}$$

$$\mathscr{M}_{22} = -\left(\mathscr{S}_1 + 2\frac{\mathscr{S}_2}{R_2}\right)\sum_{p=1}^{\mathscr{N}_\mathscr{X}}\sum_{k=1}^{\mathscr{N}_\mathscr{Y}} \mathbb{i}_{sp}^{\mathscr{X}}\mathbb{i}_{pk}^{\mathscr{Y}}\mathscr{V}_{kj}$$

$$\mathscr{M}_{25} = -\left(\mathscr{S}_2 + \frac{\mathscr{S}_3}{R_2}\right)\sum_{p=1}^{\mathscr{N}_\mathscr{X}}\sum_{k=1}^{\mathscr{N}_\mathscr{Y}} \mathbb{i}_{sp}^{\mathscr{X}}\mathbb{i}_{pk}^{\mathscr{Y}}\mathscr{f}_{\mathscr{Y}kj}$$

$$\mathscr{M}_{33} = -\mathscr{S}_1\sum_{p=1}^{\mathscr{N}_\mathscr{X}}\sum_{k=1}^{\mathscr{N}_\mathscr{Y}} \mathbb{i}_{sp}^{\mathscr{X}}\mathbb{i}_{pk}^{\mathscr{Y}}\mathscr{W}_{kj}$$

$$\mathscr{M}_{41} = -\left(\mathscr{S}_2 + \frac{\mathscr{S}_3}{R_1}\right)\sum_{p=1}^{\mathscr{N}_\mathscr{X}}\sum_{k=1}^{\mathscr{N}_\mathscr{Y}} \mathbb{i}_{sp}^{\mathscr{X}}\mathbb{i}_{pk}^{\mathscr{Y}}\mathscr{U}_{kj}$$

$$\mathscr{M}_{25} = -\left(\mathscr{S}_2 + \frac{\mathscr{S}_3}{R_2}\right)\sum_{p=1}^{\mathscr{N}_\mathscr{X}}\sum_{k=1}^{\mathscr{N}_\mathscr{Y}} \mathbb{i}_{sp}^{\mathscr{X}}\mathbb{i}_{pk}^{\mathscr{Y}}\mathscr{f}_{\mathscr{Y}kj}$$

$$\mathscr{M}_{44} = -\mathscr{S}_3\sum_{p=1}^{\mathscr{N}_\mathscr{X}}\sum_{k=1}^{\mathscr{N}_\mathscr{Y}} \mathbb{i}_{sp}^{\mathscr{X}}\mathbb{i}_{pk}^{\mathscr{Y}}\mathscr{f}_{\mathscr{X}kj}$$

$$\mathscr{M}_{55} = -\mathscr{S}_3\sum_{p=1}^{\mathscr{N}_\mathscr{X}}\sum_{k=1}^{\mathscr{N}_\mathscr{Y}} \mathbb{i}_{sp}^{\mathscr{X}}\mathbb{i}_{pk}^{\mathscr{Y}}\mathscr{f}_{\mathscr{Y}kj}$$

Other $\mathscr{M}_{ij}$ are equal to zero.

A.2. Elements of the stiffness matrix

(For simplicity the superscript $\mathfrak{YY}$ is dropped out)

$$\mathscr{K}_{11} = \mathscr{A}_{11}\sum_{p=1}^{\mathscr{N}_\mathscr{X}}\sum_{k=1}^{\mathscr{N}_\mathscr{Y}} \mathfrak{L}_{sp}^{\mathscr{X}}\mathbb{i}_{pk}^{\mathscr{Y}}\mathscr{U}_{kj} + \mathscr{A}_{66}\sum_{p=1}^{\mathscr{N}_\mathscr{X}}\sum_{k=1}^{\mathscr{N}_\mathscr{Y}} \mathbb{i}_{sp}^{\mathscr{X}}\mathfrak{L}_{pk}^{\mathscr{Y}}\mathscr{U}_{kj} + c_0^2D_{66}\sum_{p=1}^{\mathscr{N}_\mathscr{X}}\sum_{k=1}^{\mathscr{N}_\mathscr{Y}} \mathbb{i}_{sp}^{\mathscr{X}}\mathfrak{L}_{pk}^{\mathscr{Y}}\mathscr{U}_{kj} - \frac{\mathscr{A}_{55}}{R_1^2}\sum_{p=1}^{\mathscr{N}_\mathscr{X}}\sum_{k=1}^{\mathscr{N}_\mathscr{Y}} \mathbb{i}_{sp}^{\mathscr{X}}\mathbb{i}_{pk}^{\mathscr{Y}}\mathscr{U}_{kj} + 2c_0B_{66}\sum_{p=1}^{\mathscr{N}_\mathscr{X}}\sum_{k=1}^{\mathscr{N}_\mathscr{Y}} \mathbb{i}_{sp}^{\mathscr{X}}\mathfrak{L}_{pk}^{\mathscr{Y}}\mathscr{U}_{kj}$$

$$\mathscr{K}_{12} = \left(\mathscr{A}_{12} + \mathscr{A}_{66} - c_0^2D_{66}\right)\sum_{p=1}^{\mathscr{N}_\mathscr{X}}\sum_{k=1}^{\mathscr{N}_\mathscr{Y}} \mathfrak{R}_{sp}^{\mathscr{X}}\mathfrak{R}_{pk}^{\mathscr{Y}}\mathscr{V}_{kj}$$

$$\mathscr{K}_{13} = \left(\frac{\mathscr{A}_{11}}{R_1} + \frac{\mathscr{A}_{12}}{R_2} + \frac{\mathscr{A}_{55}}{R_1}\right)\sum_{p=1}^{\mathscr{N}_\mathscr{X}}\sum_{k=1}^{\mathscr{N}_\mathscr{Y}} \mathfrak{R}_{sp}^{\mathscr{X}}\mathbb{i}_{pk}^{\mathscr{Y}}\mathscr{W}_{kj}$$

$$\mathscr{K}_{14} = B_{11}\sum_{p=1}^{\mathscr{N}_\mathscr{X}}\sum_{k=1}^{\mathscr{N}_\mathscr{Y}} \mathfrak{L}_{sp}^{\mathscr{X}}\mathbb{i}_{pk}^{\mathscr{Y}}\mathscr{f}_{\mathscr{X}kj} + B_{66}\sum_{p=1}^{\mathscr{N}_\mathscr{X}}\sum_{k=1}^{\mathscr{N}_\mathscr{Y}} \mathbb{i}_{sp}^{\mathscr{X}}\mathfrak{L}_{pk}^{\mathscr{Y}}\mathscr{f}_{\mathscr{X}kj} + c_0D_{66}\sum_{p=1}^{\mathscr{N}_\mathscr{X}}\sum_{k=1}^{\mathscr{N}_\mathscr{Y}} \mathbb{i}_{sp}^{\mathscr{X}}\mathfrak{L}_{pk}^{\mathscr{Y}}\mathscr{f}_{\mathscr{X}kj} + \frac{\mathscr{A}_{55}}{R_1}\sum_{p=1}^{\mathscr{N}_\mathscr{X}}\sum_{k=1}^{\mathscr{N}_\mathscr{Y}} \mathbb{i}_{sp}^{\mathscr{X}}\mathbb{i}_{pk}^{\mathscr{Y}}\mathscr{f}_{\mathscr{X}kj},$$

$$\mathscr{K}_{15} = \left(B_{12} + B_{66} + c_0D_{66}\right)\sum_{p=1}^{\mathscr{N}_\mathscr{X}}\sum_{k=1}^{\mathscr{N}_\mathscr{Y}} \mathfrak{R}_{sp}^{\mathscr{X}}\mathfrak{R}_{pk}^{\mathscr{Y}}\mathscr{f}_{\mathscr{Y}kj}$$

$$\mathscr{K}_{21} = \left(\mathscr{A}_{12} + \mathscr{A}_{66} - c_0^2D_{66}\right)\sum_{p=1}^{\mathscr{N}_\mathscr{X}}\sum_{k=1}^{\mathscr{N}_\mathscr{Y}} \mathfrak{R}_{sp}^{\mathscr{X}}\mathfrak{R}_{pk}^{\mathscr{Y}}\mathscr{U}_{kj}$$

$$\mathscr{K}_{22} = \mathscr{A}_{66}\sum_{p=1}^{\mathscr{N}_\mathscr{X}}\sum_{k=1}^{\mathscr{N}_\mathscr{Y}} \mathfrak{L}_{sp}^{\mathscr{X}}\mathbb{i}_{pk}^{\mathscr{Y}}\mathscr{V}_{kj} + \mathscr{A}_{22}\sum_{p=1}^{\mathscr{N}_\mathscr{X}}\sum_{k=1}^{\mathscr{N}_\mathscr{Y}} \mathbb{i}_{sp}^{\mathscr{X}}\mathfrak{L}_{pk}^{\mathscr{Y}}\mathscr{V}_{kj} + c_0^2D_{66}\sum_{p=1}^{\mathscr{N}_\mathscr{X}}\sum_{k=1}^{\mathscr{N}_\mathscr{Y}} \mathfrak{L}_{sp}^{\mathscr{X}}\mathbb{i}_{pk}^{\mathscr{Y}}\mathscr{V}_{kj} - \frac{\mathscr{A}_{44}}{R_2^2}\sum_{p=1}^{\mathscr{N}_\mathscr{X}}\sum_{k=1}^{\mathscr{N}_\mathscr{Y}} \mathbb{i}_{sp}^{\mathscr{X}}\mathbb{i}_{pk}^{\mathscr{Y}}\mathscr{V}_{kj} - 2c_0B_{66}\sum_{p=1}^{\mathscr{N}_\mathscr{X}}\sum_{k=1}^{\mathscr{N}_\mathscr{Y}} \mathfrak{L}_{sp}^{\mathscr{X}}\mathbb{i}_{pk}^{\mathscr{Y}}\mathscr{V}_{kj}$$

$$\mathscr{K}_{23} = \left(\frac{\mathscr{A}_{12}}{R_1} + \frac{\mathscr{A}_{22}}{R_2} + \frac{\mathscr{A}_{44}}{R_2}\right)\sum_{p=1}^{\mathscr{N}_\mathscr{X}}\sum_{k=1}^{\mathscr{N}_\mathscr{Y}} \mathbb{i}_{sp}^{\mathscr{X}}\mathfrak{R}_{pk}^{\mathscr{Y}}\mathscr{W}_{kj}$$

$$\mathscr{K}_{24} = (B_{12} + B_{66} - c_0 D_{66}) \sum_{p=1}^{\mathscr{N}_\mathscr{X}} \sum_{k=1}^{\mathscr{N}_\mathscr{Y}} \mathfrak{R}_{sp}^{\mathscr{X}} \mathfrak{R}_{pk}^{\mathscr{Y}} \diagup_{\mathscr{X}kj}$$

$$\mathscr{K}_{25} = B_{66} \sum_{p=1}^{\mathscr{N}_\mathscr{X}} \sum_{k=1}^{\mathscr{N}_\mathscr{Y}} \mathfrak{L}_{sp}^{\mathscr{X}} \ddot{\imath}_{pk}^{\mathscr{Y}} \diagup_{\mathscr{Y}kj} + B_{22} \sum_{p=1}^{\mathscr{N}_\mathscr{X}} \sum_{k=1}^{\mathscr{N}_\mathscr{Y}} \ddot{\imath}_{sp}^{\mathscr{X}} \mathfrak{L}_{pk}^{\mathscr{Y}} \diagup_{\mathscr{Y}kj} - c_0 D_{66} \sum_{p=1}^{\mathscr{N}_\mathscr{X}} \sum_{k=1}^{\mathscr{N}_\mathscr{Y}} \mathfrak{L}_{sp}^{\mathscr{X}} \ddot{\imath}_{pk}^{\mathscr{Y}} \diagup_{\mathscr{Y}kj} + \frac{\mathscr{A}_{44}}{R_2} \sum_{p=1}^{\mathscr{N}_\mathscr{X}} \sum_{k=1}^{\mathscr{N}_\mathscr{Y}} \ddot{\imath}_{sp}^{\mathscr{X}} \ddot{\imath}_{pk}^{\mathscr{Y}} \diagup_{\mathscr{Y}kj},$$

$$\mathscr{K}_{31} = -\left(\frac{\mathscr{A}_{11}}{R_1} + \frac{\mathscr{A}_{12}}{R_2} + \frac{\mathscr{A}_{55}}{R_1}\right) \sum_{p=1}^{\mathscr{N}_\mathscr{X}} \sum_{k=1}^{\mathscr{N}_\mathscr{Y}} \mathfrak{R}_{sp}^{\mathscr{X}} \ddot{\imath}_{pk}^{\mathscr{Y}} \mathscr{U}_{kj}$$

$$\mathscr{K}_{32} = -\left(\frac{\mathscr{A}_{12}}{R_1} + \frac{\mathscr{A}_{22}}{R_2} + \frac{\mathscr{A}_{44}}{R_2}\right) \sum_{p=1}^{\mathscr{N}_\mathscr{X}} \sum_{k=1}^{\mathscr{N}_\mathscr{Y}} \ddot{\imath}_{sp}^{\mathscr{X}} \mathfrak{R}_{pk}^{\mathscr{Y}} \mathscr{V}_{kj}$$

$$\mathscr{K}_{33} = \mathscr{A}_{55} \sum_{p=1}^{\mathscr{N}_\mathscr{X}} \sum_{k=1}^{\mathscr{N}_\mathscr{Y}} \mathfrak{L}_{sp}^{\mathscr{X}} \ddot{\imath}_{pk}^{\mathscr{Y}} \mathscr{W}_{kj} + \mathscr{A}_{44} \sum_{p=1}^{\mathscr{N}_\mathscr{X}} \sum_{k=1}^{\mathscr{N}_\mathscr{Y}} \ddot{\imath}_{sp}^{\mathscr{X}} \mathfrak{L}_{pk}^{\mathscr{Y}} \mathscr{W}_{kj} - \frac{\mathscr{A}_{11}}{R_1^2} \sum_{p=1}^{\mathscr{N}_\mathscr{X}} \sum_{k=1}^{\mathscr{N}_\mathscr{Y}} \ddot{\imath}_{sp}^{\mathscr{X}} \ddot{\imath}_{pk}^{\mathscr{Y}} \mathscr{W}_{kj} - \frac{2\mathscr{A}_{12}}{R_1 R_2} \sum_{p=1}^{\mathscr{N}_\mathscr{X}} \sum_{k=1}^{\mathscr{N}_\mathscr{Y}} \ddot{\imath}_{sp}^{\mathscr{X}} \ddot{\imath}_{pk}^{\mathscr{Y}} \mathscr{W}_{kj} - \frac{\mathscr{A}_{22}}{R_2^2} \sum_{p=1}^{\mathscr{N}_\mathscr{X}} \sum_{k=1}^{\mathscr{N}_\mathscr{Y}} \ddot{\imath}_{sp}^{\mathscr{X}} \ddot{\imath}_{pk}^{\mathscr{Y}} \mathscr{W}_{kj}$$

$$\mathscr{K}_{34} = -\left(\frac{B_{11}}{R_1} + \frac{B_{12}}{R_2} - \mathscr{A}_{55}\right) \sum_{p=1}^{\mathscr{N}_\mathscr{X}} \sum_{k=1}^{\mathscr{N}_\mathscr{Y}} \mathfrak{R}_{sp}^{\mathscr{X}} \ddot{\imath}_{pk}^{\mathscr{Y}} \diagup_{\mathscr{X}kj}$$

$$\mathscr{K}_{35} = -\left(\frac{B_{12}}{R_1} + \frac{B_{22}}{R_2} - \mathscr{A}_{44}\right) \sum_{p=1}^{\mathscr{N}_\mathscr{X}} \sum_{k=1}^{\mathscr{N}_\mathscr{Y}} \ddot{\imath}_{sp}^{\mathscr{X}} \mathfrak{R}_{pk}^{\mathscr{Y}} \diagup_{\mathscr{Y}kj}$$

$$\mathscr{K}_{41} = B_{11} \sum_{p=1}^{\mathscr{N}_\mathscr{X}} \sum_{k=1}^{\mathscr{N}_\mathscr{Y}} \mathfrak{L}_{sp}^{\mathscr{X}} \ddot{\imath}_{pk}^{\mathscr{Y}} \mathscr{U}_{kj} + B_{66} \sum_{p=1}^{\mathscr{N}_\mathscr{X}} \sum_{k=1}^{\mathscr{N}_\mathscr{Y}} \ddot{\imath}_{sp}^{\mathscr{X}} \mathfrak{L}_{pk}^{\mathscr{Y}} \mathscr{U}_{kj} + c_0 D_{66} \sum_{p=1}^{\mathscr{N}_\mathscr{X}} \sum_{k=1}^{\mathscr{N}_\mathscr{Y}} \ddot{\imath}_{sp}^{\mathscr{X}} \mathfrak{L}_{pk}^{\mathscr{Y}} \mathscr{U}_{kj} + \frac{\mathscr{A}_{55}}{R_1} \sum_{p=1}^{\mathscr{N}_\mathscr{X}} \sum_{k=1}^{\mathscr{N}_\mathscr{Y}} \ddot{\imath}_{sp}^{\mathscr{X}} \ddot{\imath}_{pk}^{\mathscr{Y}} \mathscr{U}_{kj}$$

$$\mathscr{K}_{42} = (B_{12} + B_{66} - c_0 D_{66}) \sum_{p=1}^{\mathscr{N}_\mathscr{X}} \sum_{k=1}^{\mathscr{N}_\mathscr{Y}} \mathfrak{R}_{sp}^{\mathscr{X}} \mathfrak{R}_{pk}^{\mathscr{Y}} \mathscr{V}_{kj}$$

$$\mathscr{K}_{43} = \left(\frac{B_{11}}{R_1} + \frac{B_{12}}{R_2} - \mathscr{A}_{55}\right) \sum_{p=1}^{\mathscr{N}_\mathscr{X}} \sum_{k=1}^{\mathscr{N}_\mathscr{Y}} \mathfrak{R}_{sp}^{\mathscr{X}} \ddot{\imath}_{pk}^{\mathscr{Y}} \mathscr{W}_{kj}$$

$$\mathscr{K}_{44} = D_{11} \sum_{p=1}^{\mathscr{N}_\mathscr{X}} \sum_{k=1}^{\mathscr{N}_\mathscr{Y}} \mathfrak{L}_{sp}^{\mathscr{X}} \ddot{\imath}_{pk}^{\mathscr{Y}} \diagup_{\mathscr{X}kj} + D_{66} \sum_{p=1}^{\mathscr{N}_\mathscr{X}} \sum_{k=1}^{\mathscr{N}_\mathscr{Y}} \ddot{\imath}_{sp}^{\mathscr{X}} \mathfrak{L}_{pk}^{\mathscr{Y}} \diagup_{\mathscr{X}kj} - \mathscr{A}_{55} \sum_{p=1}^{\mathscr{N}_\mathscr{X}} \sum_{k=1}^{\mathscr{N}_\mathscr{Y}} \ddot{\imath}_{sp}^{\mathscr{X}} \ddot{\imath}_{pk}^{\mathscr{Y}} \diagup_{\mathscr{X}kj}$$

$$\mathscr{K}_{45} = (D_{12} + D_{66}) \sum_{p=1}^{\mathscr{N}_\mathscr{X}} \sum_{k=1}^{\mathscr{N}_\mathscr{Y}} \mathfrak{R}_{sp}^{\mathscr{X}} \mathfrak{R}_{pk}^{\mathscr{Y}} \diagup_{\mathscr{Y}kj}$$

$$\mathscr{K}_{51} = (B_{12} + B_{66} + c_0 D_{66}) \sum_{p=1}^{\mathscr{N}_\mathscr{X}} \sum_{k=1}^{\mathscr{N}_\mathscr{Y}} \mathfrak{R}_{sp}^{\mathscr{X}} \mathfrak{R}_{pk}^{\mathscr{Y}} \mathscr{U}_{kj}$$

$$\mathscr{K}_{52} = B_{66} \sum_{p=1}^{\mathscr{N}_\mathscr{X}} \sum_{k=1}^{\mathscr{N}_\mathscr{Y}} \mathfrak{L}_{sp}^{\mathscr{X}} \ddot{\imath}_{pk}^{\mathscr{Y}} \mathscr{V}_{kj} + B_{22} \sum_{p=1}^{\mathscr{N}_\mathscr{X}} \sum_{k=1}^{\mathscr{N}_\mathscr{Y}} \ddot{\imath}_{sp}^{\mathscr{X}} \mathfrak{L}_{pk}^{\mathscr{Y}} \mathscr{V}_{kj} - c_0 D_{66} \sum_{p=1}^{\mathscr{N}_\mathscr{X}} \sum_{k=1}^{\mathscr{N}_\mathscr{Y}} \mathfrak{L}_{sp}^{\mathscr{X}} \ddot{\imath}_{pk}^{\mathscr{Y}} \mathscr{V}_{kj} + \frac{\mathscr{A}_{44}}{R_2} \sum_{p=1}^{\mathscr{N}_\mathscr{X}} \sum_{k=1}^{\mathscr{N}_\mathscr{Y}} \ddot{\imath}_{sp}^{\mathscr{X}} \ddot{\imath}_{pk}^{\mathscr{Y}} \mathscr{V}_{kj}$$

$$\mathscr{K}_{53} = \left(\frac{B_{12}}{R_1} + \frac{B_{22}}{R_2} - \mathscr{A}_{44}\right) \sum_{p=1}^{\mathscr{N}_\mathscr{X}} \sum_{k=1}^{\mathscr{N}_\mathscr{Y}} \ddot{\imath}_{sp}^{\mathscr{X}} \mathfrak{R}_{pk}^{\mathscr{Y}} \mathscr{W}_{kj}$$

$$\mathscr{K}_{54} = (D_{12} + D_{66}) \sum_{p=1}^{\mathscr{N}_\mathscr{X}} \sum_{k=1}^{\mathscr{N}_\mathscr{Y}} \mathfrak{R}_{sp}^{\mathscr{X}} \mathfrak{R}_{pk}^{\mathscr{Y}} \diagup_{\mathscr{X}kj}$$

$$\mathscr{K}_{55} = D_{66} \sum_{p=1}^{\mathscr{N}_\mathscr{X}} \sum_{k=1}^{\mathscr{N}_\mathscr{Y}} \mathfrak{L}_{sp}^{\mathscr{X}} \ddot{\imath}_{pk}^{\mathscr{Y}} \diagup_{\mathscr{Y}kj} + D_{22} \sum_{p=1}^{\mathscr{N}_\mathscr{X}} \sum_{k=1}^{\mathscr{N}_\mathscr{Y}} \ddot{\imath}_{sp}^{\mathscr{X}} \mathfrak{L}_{pk}^{\mathscr{Y}} \diagup_{\mathscr{Y}kj} - \mathscr{A}_{44} \sum_{p=1}^{\mathscr{N}_\mathscr{X}} \sum_{k=1}^{\mathscr{N}_\mathscr{Y}} \ddot{\imath}_{sp}^{\mathscr{X}} \ddot{\imath}_{pk}^{\mathscr{Y}} \diagup_{\mathscr{Y}kj}$$

A.3. Elements of the piezoelectric matrix
(For simplicity the superscript $\mathfrak{Y}\mathfrak{X}$ is dropped out)

$$\mathscr{K}_{11} = -e_{31}^{a} H_1^{a} \lambda_m \sum_{p=1}^{\mathscr{N}_\mathscr{X}} \sum_{k=1}^{\mathscr{N}_\mathscr{Y}} \mathfrak{R}_{sp}^{\mathscr{X}} \ddot{\imath}_{pk}^{\mathscr{Y}} \mathscr{U}_{kj}$$

$$\mathscr{K}_{12} = -e_{32}^{a} H_1^a \mu_n \sum_{p=1}^{\mathscr{N}_{\mathscr{X}}} \sum_{k=1}^{\mathscr{N}_{\mathscr{Y}}} \mathbb{i}_{sp}^{\mathscr{X}} \Re_{pk}^{\mathscr{Y}} \mathscr{V}_{kj}$$

$$\mathscr{K}_{13} = -\left(\frac{e_{31}^{a}}{R_1} + \frac{e_{32}^{a}}{R_2}\right) \sum_{p=1}^{\mathscr{N}_{\mathscr{X}}} \sum_{k=1}^{\mathscr{N}_{\mathscr{Y}}} \mathbb{i}_{sp}^{\mathscr{X}} \mathbb{i}_{pk}^{\mathscr{Y}} \mathscr{W}_{kj}$$

$$\mathscr{K}_{14} = -e_{31}^{a} H_2^a \lambda_m \sum_{p=1}^{\mathscr{N}_{\mathscr{X}}} \sum_{k=1}^{\mathscr{N}_{\mathscr{Y}}} \Re_{sp}^{\mathscr{X}} \mathbb{i}_{pk}^{\mathscr{Y}} \mathscr{F}_{\mathscr{X}kj}$$

$$\mathscr{K}_{15} = -e_{32}^{a} H_2^a \mu_n \sum_{p=1}^{\mathscr{N}_{\mathscr{X}}} \sum_{k=1}^{\mathscr{N}_{\mathscr{Y}}} \mathbb{i}_{sp}^{\mathscr{X}} \Re_{pk}^{\mathscr{Y}} \mathscr{F}_{\mathscr{Y}kj}$$

$$\mathscr{K}_{21} = -e_{31}^{s} H_1^s \lambda_m \sum_{p=1}^{\mathscr{N}_{\mathscr{X}}} \sum_{k=1}^{\mathscr{N}_{\mathscr{Y}}} \Re_{sp}^{\mathscr{X}} \mathbb{i}_{pk}^{\mathscr{Y}} \mathscr{U}_{kj}$$

$$\mathscr{K}_{22} = -e_{32}^{s} H_1^s \mu_n \sum_{p=1}^{\mathscr{N}_{\mathscr{X}}} \sum_{k=1}^{\mathscr{N}_{\mathscr{Y}}} \mathbb{i}_{sp}^{\mathscr{X}} \Re_{pk}^{\mathscr{Y}} \mathscr{V}_{kj}$$

$$\mathscr{K}_{23} = -\left(\frac{e_{31}^{s}}{R_1} + \frac{e_{32}^{s}}{R_2}\right) \sum_{p=1}^{\mathscr{N}_{\mathscr{X}}} \sum_{k=1}^{\mathscr{N}_{\mathscr{Y}}} \mathbb{i}_{sp}^{\mathscr{X}} \mathbb{i}_{pk}^{\mathscr{Y}} \mathscr{W}_{kj}$$

$$\mathscr{K}_{24} = -e_{31}^{s} H_2^s \lambda_m \sum_{p=1}^{\mathscr{N}_{\mathscr{X}}} \sum_{k=1}^{\mathscr{N}_{\mathscr{Y}}} \Re_{sp}^{\mathscr{X}} \mathbb{i}_{pk}^{\mathscr{Y}} \mathscr{F}_{\mathscr{X}kj}$$

$$\mathscr{K}_{25} = -e_{32}^{s} H_2^s \mu_n \sum_{p=1}^{\mathscr{N}_{\mathscr{X}}} \sum_{k=1}^{\mathscr{N}_{\mathscr{Y}}} \mathbb{i}_{sp}^{\mathscr{X}} \Re_{pk}^{\mathscr{Y}} \mathscr{F}_{\mathscr{Y}kj}$$

A.4. Elements of the permittivity matrix
(For simplicity the superscript $\mathfrak{X}\mathfrak{X}$ is dropped out)

$$\mathscr{K}_{11} = -\frac{\eta^a}{h^a} \sum_{p=1}^{\mathscr{N}_{\mathscr{X}}} \sum_{k=1}^{\mathscr{N}_{\mathscr{Y}}} \mathbb{i}_{sp}^{\mathscr{X}} \mathbb{i}_{pk}^{\mathscr{Y}} \Phi_{kj}^{a}$$

$$\mathscr{K}_{12} = 0$$

$$\mathscr{K}_{21} = 0$$

$$\mathscr{K}_{22} = -\frac{\eta^s}{h^s} \sum_{p=1}^{\mathscr{N}_{\mathscr{X}}} \sum_{k=1}^{\mathscr{N}_{\mathscr{Y}}} \mathbb{i}_{sp}^{\mathscr{X}} \mathbb{i}_{pk}^{\mathscr{Y}} \Phi_{kj}^{s}$$

References

[1] C. Yang, W. Lu, Y. Xia, Reliability-constrained optimal attitude-vibration control for rigid-flexible coupling satellite using interval dimension-wise analysis, Reliability Engineering & System Safety 237 (2023) 109382.

[2] L. Wang, J. Liu, Z. Zhou, Y. Li, A two-stage dimension-reduced dynamic reliability evaluation (TD-DRE) method for vibration control structures based on interval collocation and narrow bounds theories, ISA Transactions 136 (2023) 622–639.

[3] I.C. Ng, S.Y. Wakenshaw, The Internet-of-Things: Review and research directions, International Journal of Research in Marketing 34 (2017) 3–21.

[4] A.A. Laghari, K. Wu, R.A. Laghari, M. Ali, A.A. Khan, A review and state of art of Internet of Things (IoT), Archives of Computational Methods in Engineering (2021) 1–19.

[5] L. Xing, Cascading failures in internet of things: review and perspectives on reliability and resilience, IEEE Internet of Things Journal 8 (2020) 44–64.

[6] Y. Shi, J. Shen, W. Guo, C. Li, Y. Zheng, Z. Zhao, J. Zhou, Y. Zhang, The nonlinear dynamic characteristics analysis and vibration reduction control of the shafting system of a hydropower unit, International Journal of Non-Linear Mechanics 146 (2022) 104166.

[7] F. Abbaspour, H. Arvin, M. Shahriari-kahkeshi, Nonlinear vibration control of a piezoelectric graphene sheet reinforced microplate with thermal uncertainty: Feedback linearization and sliding mode approaches, Thin-Walled Structures 181 (2022) 110129.

[8] N.A. Saeed, E. Mahrous, E. Abouel Nasr, J. Awrejcewicz, Nonlinear dynamics and motion bifurcations of the rotor active magnetic bearings system with a new control scheme and rub-impact force, Symmetry 13 (2021) 1502.

[9] J. Mondal, S. Chatterjee, Controlling self-excited vibration of a nonlinear beam by nonlinear resonant velocity feedback with time-delay, International Journal of Non-Linear Mechanics 131 (2021) 103684.

[10] Y. Lu, Q. Shao, M. Amabili, H. Yue, H. Guo, Nonlinear vibration control effects of membrane structures with in-plane PVDF actuators: A parametric study, International Journal of Non-Linear Mechanics 122 (2020) 103466.

[11] H. Bauomy, A. El-Sayed, A new six-degrees of freedom model designed for a composite plate through PPF controllers, Applied Mathematical Modelling 88 (2020) 604–630.

[12] Y.S. Hamed, A. El Shehry, M. Sayed, Nonlinear modified positive position feedback control of cantilever beam system carrying an intermediate lumped mass, Alexandria Engineering Journal 59 (2020) 3847–3862.

[13] T. He, G.G. Zhu, S.S.-M. Swei, W. Su, Smooth-switching LPV control for vibration suppression of a flexible airplane wing, Aerospace Science and Technology 84 (2019) 895–903.

[14] G. Zhao, A. Paknejad, G. Raze, A. Deraemaeker, G. Kerschen, C. Collette, Nonlinear positive position feedback control for mitigation of nonlinear vibrations, Mechanical Systems and Signal Processing 132 (2019) 457–470.

[15] S. Lu, Y. Jiang, W. Zhang, X. Song, Vibration suppression of cantilevered piezoelectric laminated composite rectangular plate subjected to aerodynamic force in hygrothermal environment, European Journal of Mechanics-A/Solids 83 (2020) 104002.

[16] C. Zhu, X. Fang, J. Liu, G. Nie, Smart control of large amplitude vibration of porous piezoelectric conical sandwich panels resting on nonlinear elastic foundation, Composite Structures 246 (2020) 112384.
[17] Y. Jiang, W. Zhang, Y. Zhang, S. Lu, Nonlinear vibrations of four-degrees of freedom for piezoelectric functionally graded graphene-reinforced laminated composite cantilever rectangular plate with PPF control strategy, Thin-Walled Structures 188 (2023) 110830.
[18] W. Hu, Y. Gao, B. Yang, Semi-active vibration control of two flexible plates using an innovative joint mechanism, Mechanical Systems and Signal Processing 130 (2019) 565–584.
[19] W. Tian, T. Zhao, Y. Gu, Z. Yang, Nonlinear flutter suppression and performance evaluation of periodically embedded nonlinear vibration absorbers in a supersonic FGM plate, Aerospace Science and Technology 121 (2022) 107198.
[20] V. Mahesh, Active control of nonlinear coupled transient vibrations of multifunctional sandwich plates with agglomerated FG-CNTs core/magneto-electro-elastic facesheets, Thin-Walled Structures 179 (2022) 109547.
[21] J. Zhao, Z. Gao, H. Li, P.K. Wong, Z. Xie, Semi-active control for the nonlinear vibration suppression of square-celled sandwich plate with multi-zone MRE filler core, Mechanical Systems and Signal Processing 172 (2022) 108953.
[22] P.K. Sahoo, S. Chatterjee, Nonlinear dynamics and control of galloping vibration under unsteady wind flow by high-frequency excitation, Communications in Nonlinear Science and Numerical Simulation 116 (2023) 106897.
[23] Y.H. Elmoghazy, B. Safaei, S. Sahmani, Finite element analysis for dynamic response of viscoelastic sandwiched structures integrated with aluminum sheets, Facta Universitatis, Series: Mechanical Engineering 21 (2023) 591–614.
[24] S. Sahmani, B. Safaei, T. Rabczuk, On the role of nonlocal strain gradient elasticity in nonlinear buckling of FG porous reinforced curved nanobeams having different degrees of curvature, International Journal of Structural Stability and Dynamics (2024).
[25] B. Safaei, E.C. Onyibo, M. Goren, K. Kotrasova, Z. Yang, S. Arman, M. Asmael, Free vibration investigation on RVE of proposed honeycomb sandwich beam and material selection optimization, Facta Universitatis, Series: Mechanical Engineering 21 (2023) 031–050.
[26] B. Safaei, E.C. Onyibo, D. Hurdoganoglu, Effect of static and harmonic loading on the honeycomb sandwich beam by using finite element method, Facta Universitatis, Series: Mechanical Engineering 20 (2022) 279–306.
[27] B. Safaei, Frequency-dependent damped vibrations of multifunctional foam plates sandwiched and integrated by composite faces, The European Physical Journal Plus 136 (2021) 1–16.
[28] B. Safaei, A. Fattahi, F. Chu, Finite element study on elastic transition in platelet reinforced composites, Microsystem Technologies 24 (2018) 2663–2671.
[29] A. Fattahi, B. Safaei, N. Ahmed, A comparison for the non-classical plate model based on axial buckling of single-layered graphene sheets, The European Physical Journal Plus 134 (2019) 555.
[30] A. Fattahi, B. Safaei, Buckling analysis of CNT-reinforced beams with arbitrary boundary conditions, Microsystem Technologies 23 (2017) 5079–5091.
[31] B. Safaei, A. Fattahi, Free vibrational response of single-layered graphene sheets embedded in an elastic matrix using different nonlocal plate models, Mechanics 23 (2017) 678–687.
[32] P. Ghanati, B. Safaei, Elastic buckling analysis of polygonal thin sheets under compression, Indian Journal of Physics 93 (2019) 47–52.
[33] H.-S. Shen, A comparison of buckling and postbuckling behavior of FGM plates with piezoelectric fiber reinforced composite actuators, Composite Structures 91 (2009) 375–384.
[34] E. Thostenson, W. Li, D. Wang, Z. Ren, T. Chou, Carbon nanotube/carbon fiber hybrid multiscale composites, Journal of Applied Physics 91 (2002) 6034–6037.
[35] H.-S. Shen, Hygrothermal effects on the postbuckling of shear deformable laminated plates, International Journal of Mechanical Sciences 43 (2001) 1259–1281.
[36] J. Reddy, K. Chandrashekhara, Geometrically non-linear transient analysis of laminated, doubly curved shells, International Journal of Non-Linear Mechanics 20 (1985) 79–90.
[37] R.A. Chaudhuri, H.R. Kabir, Boundary-discontinuous Fourier analysis of doubly-curved panels using classical shallow shell theories, International Journal of Engineering Science 31 (1993) 1551–1564.
[38] J. Reddy, Exact solutions of moderately thick laminated shells, Journal of Engineering Mechanics 110 (1984) 794–809.
[39] J.N. Reddy, Mechanics of laminated composite plates and shells: theory and analysis, CRC press, 2003.
[40] K. Liew, J. Yang, S. Kitipornchai, Postbuckling of piezoelectric FGM plates subject to thermo-electro-mechanical loading, International Journal of Solids and Structures 40 (2003) 3869–3892.
[41] M. Shariyat, Dynamic buckling of suddenly loaded imperfect hybrid FGM cylindrical shells with temperature-dependent material properties under thermo-electro-mechanical loads, International Journal of Mechanical Sciences 50 (2008) 1561–1571.
[42] M. Shakeri, R. Mirzaeifar, Static and dynamic analysis of thick functionally graded plates with piezoelectric layers using layerwise finite element model, Mechanics of Advanced Materials and Structures 16 (2009) 561–575.
[43] S. Lee, J. Reddy, Vibration suppression of laminated shell structures investigated using higher order shear deformation theory, Smart Materials and Structures 13 (2004) 1176.
[44] M. Amabili, Nonlinear vibrations and stability of shells and plates, Cambridge University Press, 2008.
[45] Y. Hu, T. Yang, Magneto-thermoelastic coupled resonance characteristics of a rotating functionally graded ferromagnetic cylindrical shell under double harmonic line loads, Aerospace Science and Technology 145 (2024) 108871, https://doi.org/10.1016/j.ast.2024.108871.
[46] T.Q. Quan, V.M. Anh, N.D. Duc, Natural frequency analysis of sandwich plate with auxetic honeycomb core and CNTRC face sheets using analytical approach and artificial neural network, Aerospace Science and Technology 144 (2024) 108806. https://doi.org/10.1016/j.ast.2023.108806.
[47] H.H. Patil, J. Pitchaimani, Sound radiation characteristics of a beam under supersonic airflow and non-uniform temperature field, Aerospace Science and Technology 147 (2024) 109001, https://doi.org/10.1016/j.ast.2024.109001.
[48] K. Chandrashekhara, Free vibrations of anisotropic laminated doubly curved shells, Computers & Structures 33 (1989) 435–440.
[49] M. Shariyat, Vibration and dynamic buckling control of imperfect hybrid FGM plates with temperature-dependent material properties subjected to thermo-electro-mechanical loading conditions, Composite Structures 88 (2009) 240–252.
[50] L. Sun, Y.X. Hao, W. Zhang, H. Li, Traveling wave vibration and critical rotating speed of rotating porous metal conical shell with elastic boundary conditions, Aerospace Science and Technology 148 (2024) 109091, https://doi.org/10.1016/j.ast.2024.109091.
[51] P.H. Wan, M.S.H. Al-Furjan, R. Kolahchi, Nonlinear flutter response and reliability of supersonic smart hybrid nanocomposite rupture trapezoidal plates subjected to yawed flow using DQHFEM, Aerospace Science and Technology 145 (2024) 108862, https://doi.org/10.1016/j.ast.2023.108862.
[52] L. Chang, Y. Hu, A.E. Ragab, On the nonlinear wave propagations of improved solar cells, Aerospace Science and Technology 146 (2024) 108941, https://doi.org/10.1016/j.ast.2024.108941.
[53] F. Tornabene, Free vibration analysis of functionally graded conical, cylindrical shell and annular plate structures with a four-parameter power-law distribution, Computer Methods in Applied Mechanics and Engineering 198 (2009) 2911–2935, https://doi.org/10.1016/j.cma.2009.04.011.
[54] M. Javani, Y. Kiani, M.R. Eslami, On the free vibrations of FG-GPLRC folded plates using GDQE procedure, Composite Structures 286 (2022) 115273, https://doi.org/10.1016/j.compstruct.2022.115273.
[55] R. Mirzaeifar, H. Bahai, S. Shahab, Active control of natural frequencies of FGM plates by piezoelectric sensor/actuator pairs, Smart Materials and Structures 17 (2008) 045003.
[56] S.-N. Nguyen, M. Cho, J.-S. Kim, J.-W. Han, Improved thermo-mechanical-viscoelastic analysis of laminated composite structures via the enhanced Lo–Christensen–Wu theory in the laplace domain, Mechanics of Advanced Materials and Structures (2022) 1–17.
[57] F. Durbin, Numerical inversion of Laplace transforms: an efficient improvement to Dubner and Abate's method, The Computer Journal 17 (1974) 371–376.
[58] E. Samaniego, C. Anitescu, S. Goswami, V.M. Nguyen-Thanh, H. Guo, K. Hamdia, X. Zhuang, T. Rabczuk, An energy approach to the solution of partial differential equations in computational mechanics via machine learning: Concepts, implementation and applications, Computer Methods in Applied Mechanics and Engineering 362 (2020) 112790.
[59] X. Zhuang, H. Guo, N. Alajlan, H. Zhu, T. Rabczuk, Deep autoencoder based energy method for the bending, vibration, and buckling analysis of Kirchhoff plates with transfer learning, European Journal of Mechanics-A/Solids 87 (2021) 104225.
[60] J. Bai, G.-R. Liu, T. Rabczuk, Y. Wang, X.-Q. Feng, Y. Gu, A robust radial point interpolation method empowered with neural network solvers (RPIM-NNS) for nonlinear solid mechanics, Computer Methods in Applied Mechanics and Engineering 429 (2024) 117159.
[61] A. Ahmed, M.N. Uddin, M. Akbar, R. Salih, M.A. Khan, H. Bisheh, T. Rabczuk, Prediction of shear behavior of glass FRP bars-reinforced ultra-highperformance concrete I-shaped beams using machine learning, International Journal of Mechanics and Materials in Design (2023) 1–22.
[62] P.G. Asteris, A.D. Skentou, A. Bardhan, P. Samui, K. Pilakoutas, Predicting concrete compressive strength using hybrid ensembling of surrogate machine learning models, Cement and Concrete Research 145 (2021) 106449.
[63] R. Cook, J. Lapeyre, H. Ma, A. Kumar, Prediction of compressive strength of concrete: critical comparison of performance of a hybrid machine learning model with standalone models, Journal of Materials in Civil Engineering 31 (2019) 04019255.
[64] J.H. Friedman, Greedy function approximation: a gradient boosting machine, Annals of Statistics (2001) 1189–1232.
[65] M.S.H. Al-Furjan, M. Fereidouni, D. Sedghiyan, M. Habibi, D. won Jung, Three-dimensional frequency response of the CNT-Carbon-Fiber reinforced laminated circular/annular plates under initially stresses, Composite Structures 257 (2021) 113146, https://doi.org/10.1016/j.compstruct.2020.113146.
[66] H. Matsunaga, Free vibration and stability of functionally graded shallow shells according to a 2D higher-order deformation theory, Composite Structures 84 (2008) 132–146.
[67] N. Wattanasakulpong, A. Chaikittiratana, An analytical investigation on free vibration of FGM doubly curved shallow shells with stiffeners under thermal environment, Aerospace Science and Technology 40 (2015) 181–190.